RSC Advances

PAPER

View Article Online
View Journal | View Issue

Cite this: *RSC Adv.*, 2023, **13**, 24674

Mononuclear nickel(II)–flavonolate complexes of tetradentate tripodal 4N ligands as structural and functional models for quercetin 2,4-dioxygenase: structures, spectra, redox and dioxygenase activity†

Tamilarasan Ajaykamal and Mallayan Palaniandavar *

Three new nickel(II)-flavonolate complexes of the type [Ni(L)(fla)](ClO_4) **1–3**, where L is the tripodal 4N ligand tris(pyrid-2-ylmethyl)amine (tpa, **L1**) or (pyrid-2-ylmethyl)bis(6-methylpyrid-2-ylmethyl)amine (6-Me_2-tpa, **L2**) or tris(*N*-Et-benzimidazol-2-ylmethyl)amine (Et-ntb, **L3**), have been isolated as functional models for Ni(II)-containing quercetin 2,4-dioxygenase. Single crystal X-ray structures of **1** and **3** reveal that Ni(II) is involved in π-back bonding with flavonolate (fla^-), as evident from enhancement in C=O bond length upon coordination [H(fla), 1.232(3); **1**, 1.245(7); **3**, 1.262(8) Å]. More asymmetric chelation of fla^- in **3** than in **1** [Δd = (Ni–$O_{carbonyl}$ − Ni–$O_{enolate}$): **1**, 0.126; **3**, 0.182 Å] corresponds to lower π-delocalization in **3** with electron-releasing *N*-Et substituent. The optimized structures of **1–3** and their geometrical isomers have been computed by DFT methods. The HOMO and LUMO, both localized on Ni(II)-bound fla^-, are highly conjugated bonding π- and antibonding π*-orbitals respectively. They are located higher in energy than the Ni(II)-based MOs (HOMO−1, $d_{x^2-y^2}$; HOMO−2/6, d_{z^2}), revealing that the Ni(II)-bound fla^- rather than Ni(II) would undergo oxidation upon exposure to dioxygen. The results of computational studies, in combination with spectral and electrochemical studies, support the involvement of redox-inactive Ni(II) in π-back bonding with fla^-, tuning the π-delocalization in fla^- and hence its activation. Upon exposure to dioxygen, all the flavonolate adducts in DMF solution decompose to produce CO and depside, which then is hydrolyzed to give the corresponding acids at 70 °C. The highest rate of dioxygenase reactivity of **3** (k_{O2}: **3** (29.10 ± 0.16) > **1** (16.67 ± 0.70) > **2** (1.81 ± 0.04 × 10^{-1} M^{-1} s^{-1})), determined by monitoring the disappearance of the LMCT band in the range 440–450 nm, is ascribed to the electron-releasing *N*-Et substituent on bzim ring, which decreases the π-delocalization in fla^- and enhances its activation.

Received 18th July 2023
Accepted 1st August 2023

DOI: 10.1039/d3ra04834a

rsc.li/rsc-advances

Introduction

The Quercetin 2,4-Dioxygenase (2,4-QueD) enzymes, found in soil microorganisms, catalyze the aerobic degradation of quercetin (3,5,7,3′,4′-pentahydroxyflavone), which is mainly derived from the decomposition of plant materials and exudates of roots and leaves, *via* activation of molecular oxygen.[1] The oxygenative ring-opening and cleavage of two carbon–carbon bonds in the substrate to form the phenolic carboxylic acid esters (depside), which is further hydrolyzed to benzoic acid and salicylic acid, with concomitant release of carbon monoxide, involves a fascinating enzyme mechanism.[2] Although many experimental advances and theoretical analyses concerning these enzymes have been reported,[3,4] there are still some issues regarding their biosynthesis and catalytic activity due to variation in their active sites. Like many other metal-based enzymes, which play the most important roles in dictating the biological functions like synthesis of biomolecules, metabolic reactions and conversions and oxidative detoxifications, the native QueD enzymes use mainly type II copper[5,6] and iron[7,8] as cofactors. Also, they use many other metal ion cofactors like Mn, Co, Ni and Zn for the catalytic degradation of quercetin, and differ by the variation in percentage of metals in the active sites.[9]

In very recent times, the enzyme QueD has engrossed the attention of bioinorganic chemists, and many synthetic models have been isolated and studied to understand their enzymatic reaction mechanism, which is still imprecise and vague. The most investigated models for the dioxygenases include copper(II),[10,11] Mn(II)[12] and Fe(III)[13] flavonolate complexes. Many synthetic models for Co, Ni, Cd, Hg and Zn containing QueD enzymes[14–18] have been isolated and studied as structural and functional models of QueDs enzyme. Very recently, Grubel *et al.*

Department of Chemistry, Bharathidasan University, Tiruchirapalli 620 024, Tamil Nadu, India. E-mail: palaniandavar@bdu.ac.in; palanim51@yahoo.com; Fax: +91-431-2407043; Tel: +91-431-2407125

† Electronic supplementary information (ESI) available. CCDC 1956984 and 2039217. For ESI and crystallographic data in CIF or other electronic format see DOI: https://doi.org/10.1039/d3ra04834a

have synthesized a series of metal complexes of Mn(II), Co(II), Ni(II), Cu(II) and Zn(II) with *N*,*N*-bis(6-phenyl-pyrid-2-ylmethyl)-*N*-(pyrid-2-ylmethyl)amine (6-Ph$_2$TPA) as QueDs models to understand the chemistry behind the native enzymes.[15] Sun *et al.* have reported metal complexes of certain dipicolylamine-based ligands with the first row transition metals like Mn, Fe, Co, Ni, Cu and Zn as QueD models, and studied the catalytic dioxygenation of flavonol.[16] Metal complexes of *N*-propanoate-*N*,*N*-bis(2-pyridylmethyl)amine (HPBMPA) and *N*-methyl-propanoate-*N*,*N*-bis(2-pyridylmethyl)amine (MPBMPA) with the first row transition metals Mn, Fe, Co, Ni, and Cu and 3-hydroxyflavoneas substrate have been studied.[17] Very recently, a series of metal complexes with the ligand hydrotris(3-mesityl) pyrazolylborate and 3-hydroxyflavone has been found to show better QueD-like dioxygenation activity.[18]

Interestingly, there is one form of nickel containing 2,4-QueD isolated from *Streptomyces* sp. *FLA*, that shows the highest reactivity[9] and it is similar to that found in other nickel-containing enzymes such as acireductone dioxygenase containing nickel.[19,20] In every part of Ni(II)-QueDs, the metal is bound to three histidine-derived imidazoles and a glutamate-derived carboxylic acid in the active sites (Scheme 1).[5c,21,22]

Although many biomimetic studies on 2,4-QueD have been made, not much attention has been paid to the biomimetic study of Ni(II)-QueD which exhibits high dioxygenase activity in spite of the redox-inactivity of the metal. The X-ray structures of only a few Ni(II)-flavonolate model complexes are known but only one of the complexes shows dioxygenation activity upon exposure to UV radiation.[12,13] Very recently, a few nickel(II) complexes of the tripodal ligand 2-([bis(pyridin-2-ylmethyl) amino]methyl)-*p*/*m*-R-benzoic acid (R = *p*-OMe, *p*-Me, *m*-Br and *m*-NO$_2$) and 3-hydroxyflavone, that show structural features related to the native enzyme, have been isolated and their ability to degrade coordinated flavonolate correlates with the Lewis acidity of the metal.[23] As QueDs model, a metastable organo peroxide complex of Ni(II) has been shown to exhibit ring cleavage of flavonols.[24] Nickel(II) complexes of hydrotris(3,5-dimethyl)pyrazolylborate and 3-hydroxyflavone (HFla) as substrate analogue have been isolated and the structural changes that occur upon modification of C=O function in these complexes to obtain the corresponding C=S and C=Se analogues as QueD models have been studied and, interestingly, the complexes are found to retain dioxygenase activity.[25] Also, theoretical aspects of many model complexes have been investigated with an to better understand the enzyme activity of nickel containing QueDs.[26,27] During the preparation of this article, the Ni(II)complex of 1,4,7-trimethyl-1,4,7-triazacyclononane (Me$_3$TACN) and 3-hydroxyflavonol, which acts as a structural and functional model for the Ni(II)-QueD enzyme, has been reported.[28]

In our laboratory, we have successfully isolated and investigated diiron(III)[29] and nickel(II) complexes,[20c,30,31] which show the potential to act as bio-mimetic and bio-inspired functional models for sMMO enzymes. Now, we have synthesized and characterized a few nickel(II) complexes of tripodal 4N ligands like tris(pyridylmethyl)amine (tpa, **L1**; 6-Me$_2$-tpa, **L2**) and tris(*N*-Et-benzimidazol-2-yl-methyl)amine (*N*-Et-ntb, **L3**) and 3-hydroxyflavone (H(fla)), as structural and functional models for Ni(II)-containing 2,4-QueD enzyme (Scheme 2). While H(fla) would act as the substrate analogue for quercetin, the pyridyl and benzimidazolyl nitrogen donors of the primary ligands would mimic the three histidyl imidazole nitrogen atoms of the enzyme active site. The incorporation of electron-releasing *N*-Et substituent on the bzim ring and sterically hindering 6-methyl substituent on the pyridyl ring is expected to fine tune the electronic properties of Ni(II), and hence the dioxygenase activity. And this study is expected to throw light on the function of Glu-73 carboxylate group bound to Ni(II) in the enzyme active site. Interestingly, the X-ray structures of two of our Ni(II)-flavonolate adducts reveal that Ni(II) exhibits π-back bonding with fla$^-$ and tunes the π-delocalization in, and activation of fla$^-$ towards reaction with dioxygen. Density functional theory (DFT) computations reveal that the HOMO and LUMO, localized on the Ni(II)-bound flavonolate, possess energies higher than the metal-based MOs (HOMO–1, $d_{x^2-y^2}$; HOMO–2/6, d_{z^2}) so that the coordinated fla$^-$ rather than Ni(II) is oxidized during dioxygenation. While the incorporation of *N*-Et substituent on bzim moiety enhances the rate of quercetinase activity the sterically

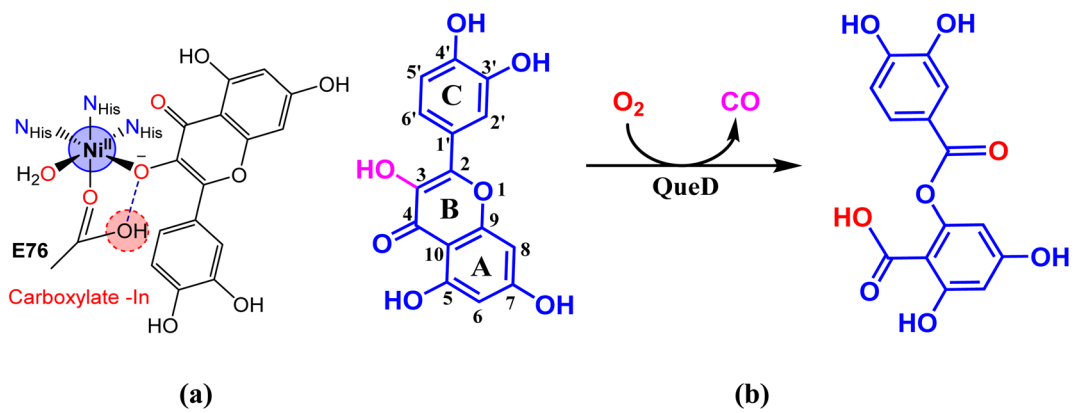

Scheme 1 (a) Active site structure of nickel(II)-derived flavonol 2,4-dioxygenase enzyme. (b) Degradation of quercetin catalyzed by the enzyme to produce depside.

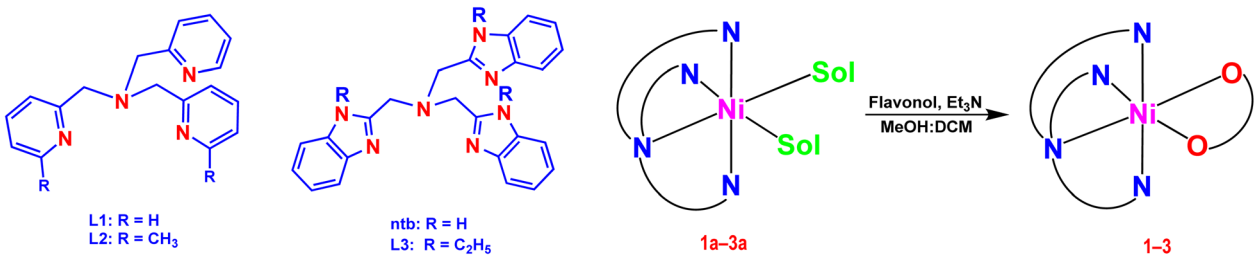

Scheme 2 Chemical structures of the ligands **L1**, **L2** and **L3** and their Ni(II) complexes $[Ni(L)(Sol)_2](ClO_4)_2$ **1a–3a** and $[Ni(L)(fla)](ClO_4)$ **1–3**.

hindering 6-Me substituent on the pyridyl ring decreases it, which is consistent with the inversion in energies of $d_{x^2-y^2}$ and d_{z^2} orbitals.

Experimental

Materials

Pyridine-2-carboxaldehyde, 6-methylpyridine-2-carboxaldehyde, 2-(aminomethyl)pyridine, nickel(II) perchlorate hexahydrate, nitrilotriacetic acid, iodoethane (Sigma-Aldrich), sodium triacetoxyborohydride, 1,2-diaminobenzene, 3-hydroxyflavone (Alfa Aesar), ethyl acetate, triethylamine, sodium sulphate (Merck, India), were used as received. Dichloromethane, diethylether, tetrahydrofuran, acetonitrile (Merck, India) and methanol, acetone (Sisco Research Laboratory, Mumbai) were distilled before use. The supporting electrolyte *tetra-N*-butylammonium perchlorate (Aldrich) was recrystallized and used.

Synthesis of ligands

The ligands tris(pyrid-2-yl-methyl)amine (tpa, **L1**),[30,32] (pyrid-2-yl-methyl)bis(6-methyl-pyrid-2-ylmethyl)amine (6-Me_2-tpa, **L2**),[30,32] and tris(benzimidazol-2-ylmethyl)amine (ntb)[30,33] were prepared by using the previously reported procedures with slight modifications. The ligand tris(*N*-et-benzimidazol-2-ylmethyl)amine (Et-ntb, **L3**) was prepared by *N*-ethylating **ntb**.

Tris(2-pyridylmethyl)amine (L1)[30,32]

The compound **L1** is a yellow solid (1.21 g, 75%). ^{1}H NMR (400 MHz, $CDCl_3$): δ = 8.43 (d, 3H), 7.54 (t, 3H), 7.50 (d, 3H), 7.04 (d), 3.79 (s, 6H) (Fig. S13 and 14†). Anal. calcd for $C_{18}H_{19}N_4$: C, 74.46; H, 6.25; N, 19.30. Found: C, 74.55; H, 6.30; N, 19.58. LC-MS (ethyl acetate) displays a peak at *m*/*z* 291.25 $[C_{18}H_{18}N_4^+]$ (calc. 291.16, Fig. S17†).

(Pyrid-2-ylmethyl)bis(6-methyl-pyrid-2-ylmethyl)amine (L2)[30,32]

The ligand **L2** is a brown solid (1.33 g, 73%). ^{1}H NMR (400 MHz, $CDCl_3$): δ = 8.60 (d, 1H), 7.74 (t, 3H), 7.24 (m, 4H), 7.04 (d, 2H), 3.79 (s, 6H), 2.45 (s, 6H). Anal. calcd for $C_{20}H_{22}N_4$: C, 75.44; H, 6.96; N, 17.60. Found: C, 75.60; H, 6.70; N, 17.78.

Tris(*N*-Et-benzimidazol-2-ylmethyl)amine (L3)

Nitrilotriacetic acid (5 g, 26.2 mmol) was ground to a fine powder and intimately mixed with 1,2-diaminobenzene (8.483 g, 78.5 mmol). The mixture was heated at 170–180 °C for 1 h at which stage effervescence had ceased. The mixture was cooled to room temperature, and the resulting red glass was taken up in dilute (~4 M) hydrochloric acid (150 mL) to obtain a greyish blue precipitate. The precipitate was filtered off and washed by slurrying it in acetone several times. The precipitate was then dissolved in water and neutralized with dilute ammonia. The off-white precipitate was collected by filtration, recrystallized from acetone, and ground to a fine powder prior to vacuum drying to give ntb (yield, 11.85 g, 87%). After thorough drying, the powder was suspended in dry tetrahydrofuran (50 mL) and stirred overnight with NaOH (3.494 g, 87.31 mmol). Iodoethane (13.62 g, 87.31 mmol) was added to this solution, and the solution left stirring for 2 days. The solvent was then stripped off to dryness and the resulting powder dissolved in chloroform. The insoluble NaBr was removed by filtration, and the filtrate was rotaevaporated to a very small volume. A little acetone was added, and upon standing crystalline reddish-brown compound **L3** was obtained (14.24 g, 86%). The compound was recrystallized and the crystals were collected and dried in vacuum. Yield, ^{1}H NMR (400 MHz, $CDC1_3$): δ = 7.68 (m, 3H), 7.16 (m, 9H), 4.21 (s, 6H), 3.37 (m, 6H), 0.67 (t, 9H) (Fig. S15 and S16†). Anal. calcd for $C_{30}H_{33}N_7$: C, 73.29; H, 6.77; N, 19.94. Found: C, 73.33; H, 6.80; N, 19.98. HR-MS (ethyl acetate) displays a peak at *m*/*z* 492.2870 $[C_{30}H_{34}N_7^+]$ (calc. 492.2870, Fig. S18†).

Isolation of Ni(II) complexes

The nickel(II) complexes were prepared by using the previously reported procedures with slight modifications.[30,31,34]

$[Ni(L1)(CH_3CN)_2](ClO_4)_2$ 1a.[30] A methanol solution (5 mL) of $Ni(ClO_4)_2 \cdot 6H_2O$ (0.365 g, 1 mmol) was added to a methanol solution (5 mL) of L1 (0.290 g, 1 mmol) under stirring at room temperature. The solution turned green in color and was stirred for an additional 30 min when light green precipitate was obtained. The precipitate was filtered off, washed with small quantities of ice-cold methanol and then dried. The precipitate was used as such for isolation of nickel–flavonolate complexes. Yield, 0.41 g, 63%. λ_{max}/nm, in ACN (ε_{max}/dm^3 mol^{-1}): 858 (280), 523 (410), 384sh. Anal. calcd for $C_{22}H_{24}N_6Cl_2NiO_8$: C, 41.94; H, 3.84; N, 13.34. Found: C, 41.77; H, 3.70; N, 13.48. HR-MS: (ACN) displays a peak at *m*/*z* 421.1179 $[M + CH_3OH - CH_3CN - 2ClO_4]^{2+}$ (calc. 421.1413, Fig. S19†).

$[Ni(L2)(CH_3CN)(H_2O)](ClO_4)_2$ 2a.[34] This was prepared by using the procedure used for preparing complex **1a** but by using

L2 ligand instead of L1. Yield, 0.48 g, 70%. λ_{max}/nm, in ACN (ε_{max}/dm^3 mol^{-1}): 936 (270), 545 (290), 428sh. Anal. calcd for $C_{22}H_{27}N_5Cl_2NiO_9$: C, 41.61; H, 4.29; N, 11.03. Found: C, 41.52; H, 4.32; N, 11.12. HR-MS: (ACN) displays a peak at *m*/*z* 575.2894 $[M + 2CH_3CN + H_2O - ClO_4]^+$ (calc. 575.1320), 603.1600 $[M + CH_3OH + 2H_2O - CH_3CN - ClO_4]^+$ (calc. 603.3206) and 447.0368 $[M + 3H_2O - CH_3CN - 2ClO_4]^{2+}$ (calc. 447.1537) (Fig. S20†).

[Ni(L3)(CH$_3$CN)$_2$](ClO$_4$)$_2$ 3a.[30,35] This was also prepared by using the procedure used for preparing complex **1a** but by using L2 ligand instead of L1. Yield, 0.62 g, 72%. λ_{max}/nm, in ACN (ε_{max}/dm^3 mol^{-1}): 932 (110), 571 (180), 361sh. Anal. calcd for $C_{34}H_{39}N_9Cl_2NiO_8$: C, 49.12; H, 4.73; N, 15.16. Found: C, 49.22; H, 4.62; N, 15.27. HR-MS: (ACN) displays a peak at *m*/*z* 648.1625 $[M - 2CH_3CN - ClO_4]^+$ (calc. 648.1636, Fig. S21†).

[Ni(L1)(fla)]ClO$_4$ 1. The complex **1a** (0.211 g, 0.5 mmol) and 3-hydroxyflavone (0.11 g, 0.5 mmol) were suspended in methanol/DCM (15 mL) and Et_3N (0.05 g, 0.5 mmol) was added with stirring. The reaction mixture was stirred for 2 h at room temperature and filtered. The residue was washed twice with MeCN and all volatiles were removed *in vacuo* to give **1** as a brown crystalline solid. Crystals of **1** suitable for single-crystal X-ray diffraction studies were obtained by slowly evaporating the volatiles from a saturated solution of **1** in acetonitrile. Yield, 0.210 g, 66%. ATR (cm^{-1}): ν(C=O), 1536; ν(C=N), 1598. λ_{max}/nm, in ACN (ε_{max}/dm^3 mol^{-1}): 929 (180), 528 (370), 441sh. Anal. calcd for $C_{33}H_{27}N_4ClNiO_7$: C, 57.80; H, 3.97; N, 8.17. Found: C, 57.68; H, 3.80; N, 8.30. HR-MS: (ACN) displays a peak at *m*/*z* 585.1432 $[M - ClO_4]^+$ (calc. 585.1437, Fig. S22†).

[Ni(L2)(fla)]ClO$_4$ 2. This complex was prepared as a brown solid by using the procedure employed for obtaining **1** and using **2a**. Yield, 0.27 g, 81%. ATR (cm^{-1}): ν(C=O), 1544; ν(C=N), 1595. λ_{max}/nm, in ACN (ε_{max}/dm^3 mol^{-1}): 1007 (170), 582 (260), 441sh. Anal. calcd for $C_{35}H_{31}N_4ClNiO_7$: C, 58.89; H, 4.38; N, 7.85. Found: C, 58.78; H, 4.47; N, 7.77. HR-MS: (ACN) displays a peak at *m*/*z* 613.1752 $[M - ClO_4]^+$ (calc. 613.1750, Fig. S23†).

[Ni(L3)(fla)]ClO$_4$ 3. This complex was prepared as a green crystalline solid by using the procedure employed for obtaining **1** and using **3a**. Crystals of **3** suitable for single-crystal X-ray diffraction studies were obtained by slowly evaporating the volatiles from a saturated solution of **3** in acetonitrile. Yield, 0.322 g, 74%. ATR (cm^{-1}): ν(C=O), 1495; ν(C=N), 1543. λ_{max}/nm, in ACN (ε_{max}/dm^3 mol^{-1}): 1022 (210), 580 (510), 446sh. Anal. calcd for $C_{45}H_{42}N_7ClNiO_{11}$: C, 54.79; H, 4.29; N, 9.94. Found: C, 54.66; H, 4.40; N, 9.82. HR-MS: (ACN) displays a peak at *m*/*z* 786.2687 $[M - ClO_4]^+$ (calc. 786.2703, Fig. S24†).

Caution!. Perchlorate salts of the compounds are potentially explosive. Only small quantities of these compounds should be prepared and suitable precautions should be taken when they are handled.

Physical methods

^{1}H and ^{13}C NMR spectra were recorded (400 and 100 MHz, respectively) on a Bruker Avance DPX 400 MHz using $CDCl_3$. Chemical shifts for proton and carbon resonances are reported for the major isomer in parts per million (d) relative to tetramethylsilane (d 0.00), chloroform (d 77.23) respectively. Multiplicities are indicated by singlet (s), doublet (d), triplet (t) and multiplet (m). FT-IR spectra of solid samples were obtained using a Bruker ATR-Alpha (Diamond) spectrophotometer. Electronic absorbance spectra were recorded in a 1 cm cuvette on a Varian Cary 300 UV-visible spectrophotometer. Kinetic measurements were recorded using a 1 cm cuvette on an Agilent diode array spectrometer (Agilent 8453). Cyclic voltammetry (CV) and differential pulse voltammetry (DPV) on glassy carbon electrode were performed in DMF at 25 °C. The voltammograms were generated using CH instruments 620C electrochemical analyzer. A three-electrode system was used to study the electrochemical behavior of complexes (0.001 M) consists of a glassy carbon working electrode (A, 0.0707 cm^2), a platinum wire auxiliary electrode and a saturated calomel reference electrode and TBAP (0.1 M) was used as the supporting electrolyte. Solutions were deoxygenated by purging with nitrogen gas for 15 min prior to the measurement. Microanalyses (C, H and N) were carried out using PR 2400 Series II PerkinElmer equipment. ESI-mass spectra were recorded using a Thermo LC-MS instrument. High resolution mass analyses were performed using electron spray ionization (ESI) technique on a Thermo Scientific Exactive plus EMR instrument. GC-MS and GC analysis were performed on Agilent 5977E GCMSD using HP-5 MS ultra-inert (30 m × 250 μm × 0.25 μm) capillary column.

Crystallographic data collection, refinement and structure solution

The molecular structures of the complexes **1** and **3** were unambiguously determined by measuring X-ray intensity data on a Bruker SMART APEX II single crystal X-ray CCD diffractometer at ambient temperature having graphite-monochromatized Mo-Kα(λ = 0.71073 Å) radiation. The data were solved using direct methods with SHELXS-97 and refined using SHELXL-97, SHELXTL and SHELXL-2014, SHELXTL.[36] The graphics interface package used was PLATON, and the figures were generated using the ORTEP 3.07 generation package.[37] The positions on all the atoms were obtained by direct methods. Metal atoms in each complex were located from the E-maps and non-hydrogen atoms were refined anisotropically. The hydrogen atoms bound to the carbon were placed in geometrically constrained positions and refined with isotropic temperature factors, generally1.2 U_{eq} of their parent atoms. Crystallographic data are listed in Tables 1, S1 and S2.†

Computational details

The coordination geometries of nickel(II) complexes with triplet spin in the ground state were fully optimized by using Density Functional Theory (DFT) at U-B3LYP level of theory by employing the Gaussian 09 program package.[38] The calculations were carried out with a mixed basis set of LANL2DZ for the nickel center, which has a relativistic effective core potential with a valence basis set, and 6-31G* for the remaining atoms.[39,40] The solvation of the complexes was carried out by employing conductor-like polarizable continuum model (CPCM) method using acetonitrile as the solvent. The normal

mode analyses were performed to check the minimal energy nature of the geometry in solution state.

Kinetic measurements

Reactivity studies. Quercetin 2,3-dioxygenase activity

The reactions of the flavonol substrate adducts $[Ni(L)(fla)]^+$ with O_2 in DMF at desired temperature were performed in a 10 mm path length UV-vis cell that was held in a Unisoku thermostated cell holder (Osaka, Japan). The solutions of the flavonolate complexes $[Ni(L)(fla)](ClO_4)$ **1–3** (1×10^{-4} M in 3 mL DMF) were maintained at 70 °C under N_2 for several minutes, and then N_2 was replaced by bubbling with O_2. The time course of the reactions was followed by monitoring the absorption spectral changes at 444–450 nm. The kinetic parameters for the catalytic dioxygenation reactions were obtained from the $\ln\{(A_t - A_\infty)/(A_0 - A_\infty)\}$ *vs.* time plot (Table 5, Fig. 7, S9–S11†) at 70 °C.

Identification of dioxygenated products[23]

In a typical experiment, deaerated 10 mL DMF solution of the flavonolate substrate adducts $[Ni(L)(fla)](ClO_4)$ **1–3** (1.0×10^{-3} M) was taken in a 50 mL RB flask, tightly closed with a rubber septum and the reaction vessel maintained at 70 °C under N_2 for several minutes by continuous bubbling of N_2 using a balloon with syringe. Then N_2 was replaced with a desired amount of dioxygen to start the reaction. The reaction mixture was taken by using a syringe periodically (*ca.* every 2 min), and the time course of the reaction was followed by monitoring the absorption spectral changes at 444–450 nm. The O_2 concentrations in DMF were calculated from literature data taking into account the partial pressure of DMF.[41]

Results and discussion

Synthesis and characterization of ligands and complexes

The ligands **L1** and **L2** were prepared by reductive amination[7b,30] which involves treating one equivalent of 2-(aminomethyl) pyridine with two equivalents of the corresponding pyridine aldehydes and using sodium triacetoxyborohydride as the reducing agent. And the benzimidazole ligand **ntb** was prepared according to a known Philips condensation reaction,[30,33] by refluxing *o*-phenylenediamine with nitrilotriacetic acid in the presence of dilute hydrochloric acid. The *N*-ethylation of **ntb** to get **L3** was carried out in dry tetrahydrofuran as a solvent by using iodoethane in the presence of NaOH.[5a,b] All the ligands were characterized by ^1H, ^{13}C NMR, elemental analysis and mass spectrometry. The 1 : 1 nickel(II) complexes **1a–3a** of the tripodal ligands **L1–L3** were prepared by adding one equivalent of the ligand to a methanol solution of an equivalent amount of $Ni(ClO_4)_2 \cdot 6H_2O$. The complexes **1–3** were prepared by adding one equivalent of 3-hydroxyflavonol in MeOH : DCM (3 : 1 v/v) solution to the complexes **1a–3a** dissolved in methanol and then adding Et_3N as base. Single crystals of **1** and **3** suitable for X-ray crystallographic analysis were obtained by slow evaporation of a $CH_3CN : CH_3OH$ solution of the complexes. The flavonolate complexes are formulated as $[Ni(L)(fla)](ClO_4)$ **1–3**, which is supported by HR-MS and the X-ray crystal structures of **1** and **3**. All the complexes with pyridyl/benzimidazolyl nitrogen donors are expected to mimic the active site environment of the substrate-bound enzyme QueDs and so they have been chosen to model the catalytic degradation reactions of the enzyme. The identity of the complexes in solution were examined by HR(ESI)-MS. All the complexes exhibit a main peak cluster at m/z (pos.) = 585.1432 for $[Ni(L1)(fla)]^+$ **1**, 613.1752 for $[Ni(L2)(fla)]^+$ **2** and 786.2687 for $[Ni(L3)(fla)]^+$ **3**. The m/z values and the isotope distribution pattern of each peak agree well with the calculated values, indicating that the complexes maintain their mononuclear structure and Ni(II) oxidation state in solution, which is consistent with other spectroscopic results. The ν(C=N) vibration observed for the pyridyl complexes **1** and **2** absorb as a strong peak around 1597 cm^{-1}, which is higher than that for the benzimidazolyl complex **3** (~1545 cm^{-1}, Fig. S2†), which is expected.[42] All the complexes show the ν(C=O) vibration of flavonolate (fla^-) as a strong peak in the range 1536–1495 cm^{-1}, which is lower than that (1602 cm^{-1}) of free flavonol, revealing that the C=O of fla^- is coordinated to Ni(II). The values of ν(C=O) varies in the order **3** < **1** < **2**, revealing that Ni(II) is involved in π-back bonding with C=O in **3** more strongly than in **1** and **2**.[11–13,18,23] Also, the decrease in ν(C=O) observed for **1** is higher than that observed for **2**, indicating that the π-back bonding of Ni(II) with C=O in the former is stronger than that in **2**. A similar decrease in ν(C=O) observed for Cu(II)-fla^- complexes has been ascribed to π-back bonding of Cu(II) with C=O of fla^- (*cf.* above).[43]

Description of X-ray crystal structures of $[Ni(L1)(fla)](ClO_4)$ 1 and $[Ni(L3)(fla)](ClO_4)$ 3

The molecular structures of complex cations of $[Ni(L1)(fla)](ClO_4)$ **1** and $[Ni(L3)(fla)](ClO_4)$ **3** are shown in Fig. 1, together with the atom numbering scheme. The principal bond lengths and bond angles of **1** and **3** are collected in Table 1. The complex cation of **1** possesses a NiN_4O_2 coordination sphere with distorted octahedral geometry constituted by all the four nitrogen atoms of the tripodal tetradentate ligand **L1**. One of the three pyridyl nitrogens (N3) and the tertiary amine nitrogen N2 of **L1** and O1 and O2 atoms of deprotonated 3-hydroxyflavonone (fla^-) occupy the corners of equatorial plane of the octahedral geometry while the other two py nitrogen atoms (N1, N4) occupy the trans axial positions. The O1 atom is coordinated trans to N2 amine nitrogen, and O2 is weakly coordinated trans to the strongly bound pyridyl N3 nitrogen. All the $Ni–N_{py}$ (Ni–N1, 2.080(5); Ni–N3, 2.050(4); Ni–N4, 2.073(6)Å) bond lengths fall in the range observed for similar complexes (Ni–N1, 2.076(10); Ni–N3, 2.056(8); Ni–N4, 2.057(9) Å).[20c,44] The $Ni–N2_{amine}$ (2.087(5) Å) bond is longer than all the three $Ni–N_{py}$ bonds, which is expected of sp^3 and sp^2 hybridizations respectively of amine and py nitrogen donors. The $Ni–O1_{enolate}$ (1.984(4) Å) bond is stronger than the $Ni–O2_{carbonyl}$ (2.110(4) Å) bond, as expected, and the bond lengths fall within the same range as those observed for similar Ni(II)-flavonolate complexes.[16,18,23] Interestingly, the C=O bond in **1** (1.245(7) Å) is longer than that (1.232(3) Å) in the free ligand H(L1).[45] This

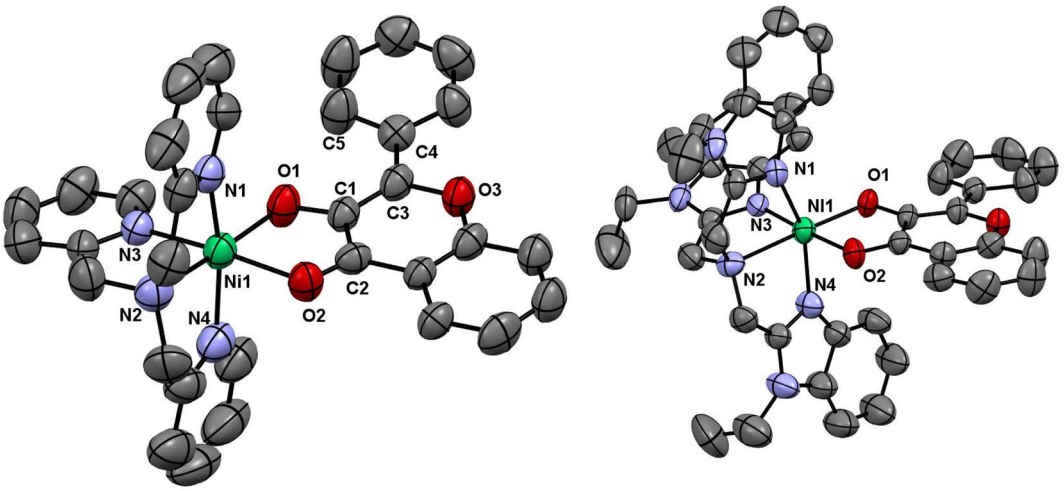

Fig. 1 ORTEP diagrams of [Ni(L1)(fla)]ClO_4 **1** and [Ni(L3)(fla)]ClO_4 **3** showing 50% probability thermal ellipsoids and labeling scheme for selected atoms. All the hydrogen atoms and perchlorate counter ions are omitted for clarity.

Table 1 Selected bond lengths [Å] for **1** and **3**

Bond lengths/Å	**1**	**3**
Ni–N1	2.080(5)	2.062(7)
Ni–N2	2.087(5)	2.221(7)
Ni–N3	2.050(4)	2.039(7)
Ni–N4	2.073(6)	2.092(7)
Ni–O1	1.984(4)	1.962(5)
Ni–O2	2.110(4)	2.144(6)
O1–C1	1.314(6)	1.302(9)
O2–C2	1.245(7)	1.262(8)
C1–C2	1.464(7)	1.498(10)

Axial donors	Equatorial donors	T′[a]	T′[a]
N1N4	N2N3O1O2	1.009	0.993
N3O2	N1N2N4O1	1.012	1.003
N2O1	N1N3N4O2	0.979	1.003

[a] $T' = \frac{(\sum \text{axial bonds})/2}{(\sum \text{equatorial bonds})/4}$.

reveals that while the filled d_{xz} and d_{yz} orbitals of Ni(II) located perpendicular to C=O bond are involved in π-back bonding with the antibonding π* orbital of C=O (*cf.* below), leading to elongation of the C=O bond, and supports the IR spectral results.

The complex cation of **3**, like its py analogue **1**, possesses a NiN_4O_2 coordination sphere with distorted octahedral geometry. The tertiary amine nitrogen atom N2 and one of the three benzimidazole (bzim) nitrogens (N3) of **L3** and O1 and O2 atoms of fla^- occupy the equatorial positions of the octahedron while the other two bzim nitrogen atoms (N1, N4) occupy the trans axial positions. All the Ni–N_{bzim} (Ni–N1, 2.062(7); Ni–N3, 2.039(7); Ni–N4, 2.092(7) Å) bond lengths are close to those observed for a similar Ni(II) complex of Me-ntb ligand.[46] The Ni–N_{amine} (2.221(7) Å) bond is longer than the Ni–N_{bzim} bonds, which is expected of sp^3 and sp^2 hybridizations respectively of amine and bzim nitrogen donors. As in **1**, the Ni–$O1_{enolate}$ (1.962(5) Å) bond is shorter than the Ni–$O2_{carbonyl}$ bond (2.144(6) Å). The Ni–N_{bzim} bonds (2.039–2.092 Å) are shorter than the corresponding Ni–N_{py} (2.050–2.080 Å) bonds in **1**, which is expected of the higher basicity of bzim nitrogen donor (pK_a: pyH^+, 5.25; 6-Me-pyH^+, 5.5; $MeImH^+$, 7.8).[47] The strongly σ-bonding bzim N-donor is expected to enhance the electron density on Ni(II), causing elongation of both Ni–$O1_{enolate}$ and Ni–$O2_{carbonyl}$ bonds. However, the former is shorter (1.962(5) Å) than that (1.984(4) Å) in the py analogue **1** while the Ni–$O2_{carbonyl}$ bond is longer, as expected. It is evident that the C=O bond oriented along the *z*-axis is involved in σ-bonding with Ni(II) ($t_{2g}^6e_g^2$) while the antibonding π* orbital of C=O is involved in π-back bonding from the filled d_{xz} and d_{yz} orbitals of Ni(II), more strongly than those in **1** (*cf.* below), causing the C=O bond in **3** (1.262(8) Å) to be longer than that in **1** (1.245(7) Å). Consequently, the π-back bonding renders the Ni–$O2_{carbonyl}$ bond (2.144(4) Å) weaker than that (2.110(4) Å) in **1**, the Ni–$O1_{enolate}$ bond stronger synergistically, and the C2–C1 bond weaker (**3**: 1.498(10) Å; **1**: 1.464(7) Å). Also, interestingly, the difference in Ni–$O1_{enolate}$ and Ni–$O2_{carbonyl}$ bonds in **3** (Δ*d*, 0.182 Å) is higher than that in **1** (0.126 Å), revealing that the –CO–C(OH)– group in **3** is coordinated more asymmetrically, and the π-conjugated carbonyl form is stabilized more than the π-delocalized aromatic form of fla^- (Scheme 3a and b, *cf.* below) or simply the π-delocalization in fla^- decreases. Hence, the shorter the Ni–$O1_{enolate}$ bond and longer the Ni–$O2_{carbonyl}$ bond or higher the asymmetry in coordination of flavonolate (fla^-), as given by the difference in Ni–O1 and Ni–O2 bond lengths (Δ*d*), the lower the π-delocalization (decrease in aromatic character) in fla^-, and hence the activation of Ni(II)-bound flavonone. Similar involvement of Ni(II) in π-back bonding is evident in the X-ray crystal structures of the complex [Ni(Me_3TACN)(fla)(NO_3)]

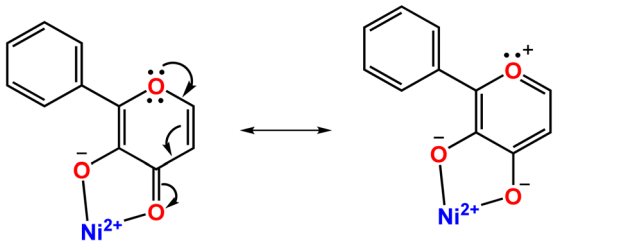

a Conjugated π-system b π-delocalized aromatic system

Scheme 3 Structures of π-conjugated carbonyl (a) and π-delocalized aromatic forms bound to nickel(II) (b).

with two geometric isomers **a** and **b**. The C=$O_{carbonyl}$ and C–$O_{enolate}$ bond lengths of both the isomers **a** (C=$O_{carbonyl}$, 1.261(18); C–$O_{enolate}$, 1.391(14) Å) and **b** (C=$O_{carbonyl}$, 1.280(20); C–$O_{enolate}$, 1.423(17) Å) are lower than those of free H(fla).[28] Also, in the X-ray crystal structures of [Ni^{II}(L)(fla)],[23] where LH is the tripodal ligand 2-([bis(pyridin-2-yl-methyl)amino]methyl)-*p*/*m*-R-benzoic acid [R = *p*-OMe and *m*-NO_2], we find that the C=O bond in the *p*-OMe complex is elongated, and the Ni–$O_{enolate}$ bond is shortened, more than the respective bonds in the parent complex. The π-back bonding of Ni(II) with C=O and synergistic σ-bonding of the enolate group to Ni(II) (C=O: –OMe, 1.253(7); –NO_2, 1.231(5); Ni–O: –OMe, 2.070(4), –NO_2, 2.062(4); Ni–O(enolate): –OMe, 2.004(4), –NO_2, 2.062(5) Å) facilitates the dioxygenation reaction of the *p*-OMe complex, rendering it more reactive. So, the highest asymmetry in coordination of fla^- and π-back bonding in **3** would be expected to lead to confer the highest rate of dioxygenation (*cf.* below).

Computational studies

A Density Functional Theory (DFT) study has been performed at the computational level of U-B3LYP/6-31G* exchange correlation functional on the Ni(II)-flavonolate complexes **1–3** to throw light on their unique structural features and to illustrate their reactivity towards dioxygen. The initial coordinates of **1** and **3** were taken from their single crystal X-ray structures and the calculated structures subjected to optimization. The structure of $[Ni(ntb)(fla)]^+$ **4** has been also computed for comparison with **3**. And the computed structural parameters (Tables 2, S4–S6, Fig. 2, S3, S4†) are in reasonably good agreement with those of the X-ray structures. So, they are valid and can be used to discuss the trends in bonding and reactivity of the model complexes. Also, we have calculated the structures of the other geometric isomers **1b–3b** (Fig. 2, Tables S3 and S7†) for $S = 0$ and $S = 1$ spin states. We found that the $S = 1$ states have energies lower than the former, which is supported by the observation of three ligand field bands (*cf.* below), and the orientation of fla^- in the distorted octahedral geometries of **1b–3b** is different from that in **1–3**. It may be noted that both such geometric isomers have been found in the X-ray structures of [$Ni(Me_3TACN)(fla)(NO_3)$].[28] The incorporation of electron-releasing *N*-Et substituent on bzim ring in **4** to get **3** (*cf.* above) renders the coordination of bzim nitrogen slightly

Table 2 Computed structural parameters and HOMO and LUMO energies and band gap energies for complexes **1–3** and $[Ni(ntb)(fla)]^+$ **4**

Bond lengths/Å	**1**	**2**	**3**	$[Ni(ntb)(fla)]^+$ **4**
Ni–N1	2.095	2.216	2.084	2.091
Ni–N2	2.149	2.114	2.260	2.279
Ni–N3	2.060	2.053	2.063	2.065
Ni–N4	2.095	2.222	2.087	2.088
Ni–O1	2.044	2.051	2.049	2.049
Ni–O2	2.113	2.099	2.119	2.112
O1–C1	1.342	1.343	1.341	1.342
O2–C2	1.297	1.297	1.295	1.296
C1–C2	1.471 (1.464)	1.467	1.473 (1.498)	1.472
Total energy (eV)	−5.136 × 10^4	−5.350 × 10^4	−6.852 × 10^4	−6.210 × 10^4
HOMO (eV)	−5.582	−5.613	−5.508	−5.528
LUMO (eV)	−2.526	−2.567	−2.480	−2.495
Band gap (eV)	3.056	3.045	3.029	3.033

Axial donors	Equatorial donors	T′[a]			
N1N4	N2N3O1O2	1.002	1.067	0.983	0.982
N3O2	N1N2N4O1	0.996	0.965	0.982	0.986
N2O1	N1N3N4O2	1.003	0.970	1.036	1.032

[a] $T' = \frac{(\sum \text{axial bonds})/2}{(\sum \text{equatorial bonds})/4}$.

stronger,[48] and the Ni–O2 bond in **3** (2.119 Å) is slightly longer than that in **4** (2.112 Å). This reveals that the stronger π-back bonding of Ni(II) with C=O in **3** results in decrease in π-delocalization in fla^- ring. In contrast, the Ni–N_{py} bonds **2** formed by the sterically hindered pyridyl nitrogen are longer than those in **1**, which results in weaker π-back bonding of Ni(II) with C=O and hence the higher π-delocalization in fla^- ring (Scheme 3b). The asymmetry in coordination of fla^-, as given by the difference in Ni–O1 and Ni–O2 bond lengths (Δd), varies as **3** (0.070) ≥ **1** (0.069) > **2** (0.048 Å), revealing that the fla^- in **1** is expected to be activated more than in **2** and to almost the same extent as in **3** (*cf.* below).

Interestingly, the doubly filled HOMO, localized on the coordinated fla^-, is higher in energy than the metal based HOMO-1, and HOMO-2/6 (Table 2, Fig. 3, 4).[49,50] This non-Aufbau electronic configuration is expected of π-conjugated molecules like H(fla), conferring enhanced stabilities on them, and such HOMO-1–HOMO inversion has been observed previously.[51] The HOMO is a highly conjugated π-MO of fla^- while the LUMO is the unoccupied highly conjugated π* orbital. The HOMO-1 and HOMO-2 are made up respectively of $d_{x^2-y^2}$ (σ*) and d_{z^2} (σ*) orbitals of Ni(II) (Fig. S3 and S4†). The observed trend in HOMO energy, H(fla) (−6.002) < **2** (−5.613) < **1** (−5.582) < **3** (−5.508 eV), is the same as that in LUMO energy, **2** (−2.567) < **1** (−2.526) < **3** (−2.480 eV), and a plot of the two energies is linear, reflecting that the 4N ligands tune the π-delocalization in fla^- (Scheme 3b). The replacement of pyridyl nitrogen donor in **1** by the more basic *N*-Et-bzim nitrogen donor to obtain **3**

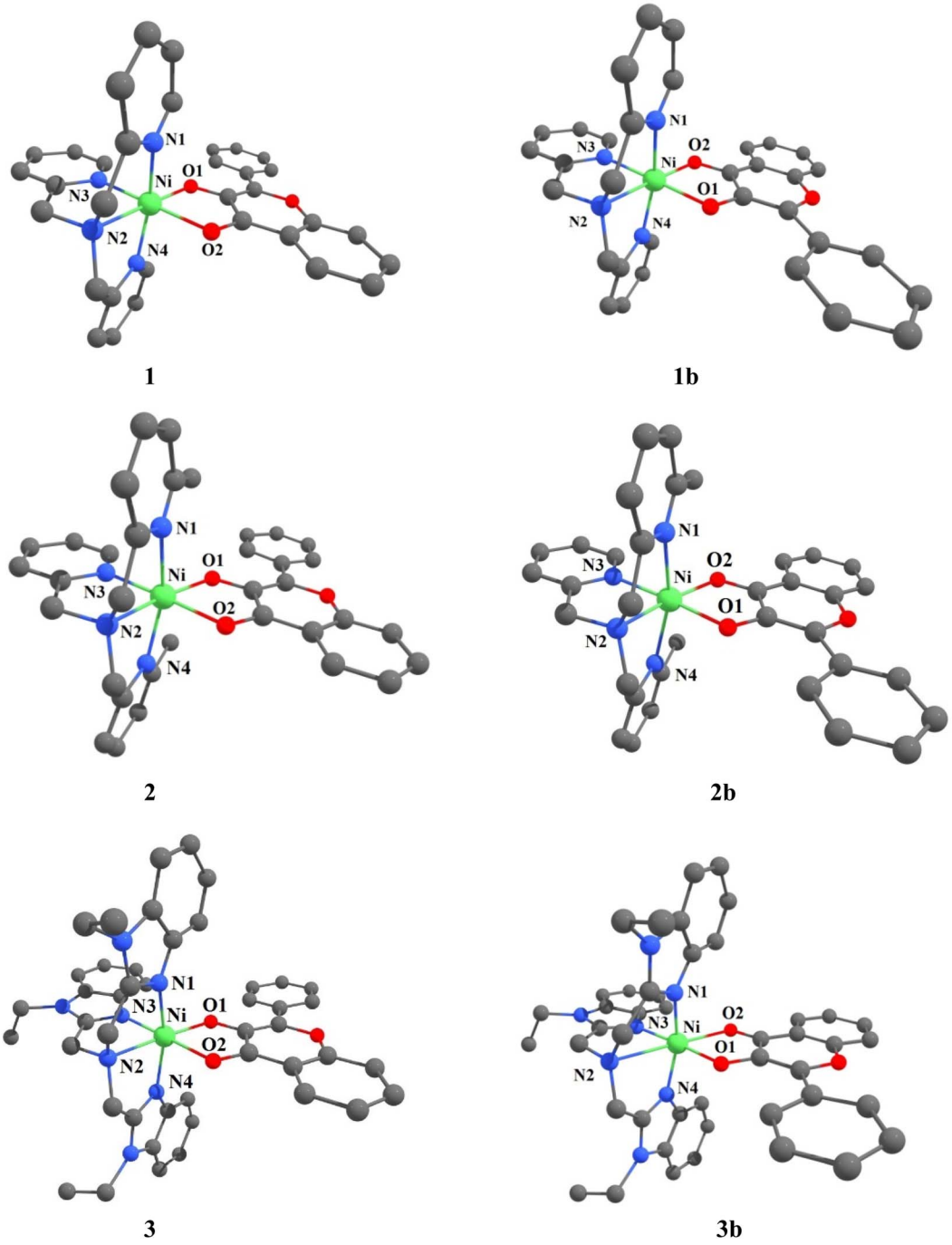

Fig. 2 Computed structures of [Ni(L)(fla)]ClO_4 **1–3** and its geometric isomer [Ni(L)(fla)]ClO_4 **1b–3b** were calculated at U-B3LYP combined correlation function and basis sets for metal atom LANL2DZ and 6-31G* basis sets for other non-metal atoms and acetonitrile as a solvent by the CPCM method.

raises the energies of both HOMO and LUMO, by enhancing the π-back bonding of Ni(II) with fla^- and decreasing the π-delocalization in fla^- in **3** (*cf.* above). On the other hand, interestingly, the inclusion of sterically hindering 6-Me group in **1** to obtain **2** increases the π-delocalization in fla^- ring in **2**, leading to a significant decrease in energies of both HOMO and LUMO, so that the HOMO-1 ($d_{x^2-y^2}$) and HOMO–2 (d_{z^2}) in **2** become higher and hence are inverted in energies. It is expected that the higher the HOMO energy the easier is the removal of electron from it and hence more facile is the oxidation of fla^-. It is seen that in **1** and **3**, the $d_{x^2-y^2}$ orbital is oriented towards N1N2N3O2 donor set while the d_{z^2} orbital is oriented towards N3O2 donor atoms. On the other hand, the d_{z^2} orbital in **2** is oriented towards N2O1 donors while the $d_{x^2-y^2}$ orbital is oriented towards N1N3N4O1 donor set, which is in accordance with the calculated values of T'.[52]

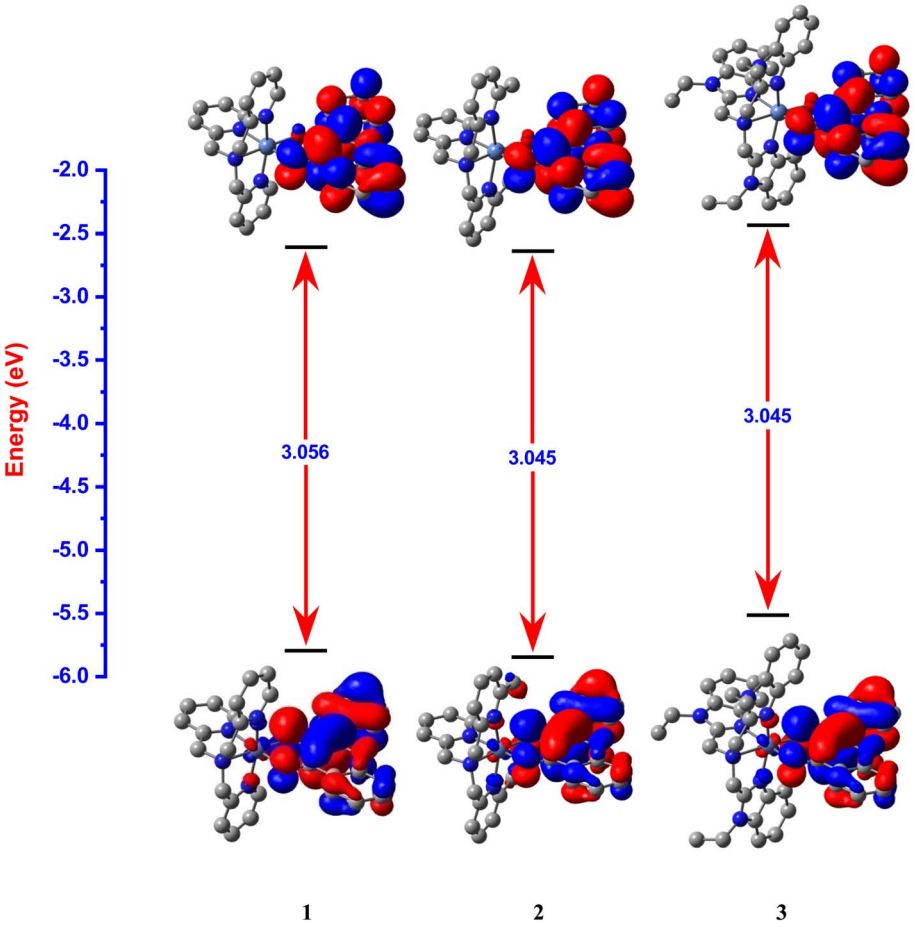

Fig. 3 HOMO and LUMO band gap energy profile diagram for $[Ni(L1)(fla)]ClO_4$ **1**, $[Ni(L2)(fla)]ClO_4$ **2** and $[Ni(L3)(fla)]ClO_4$ **3** were calculated at U-B3LYP combined correlation function and basis sets for metal atom LANL2DZ and 6-31G* basis sets for other non-metal atoms and acetonitrile as a solvent by the CPCM method.

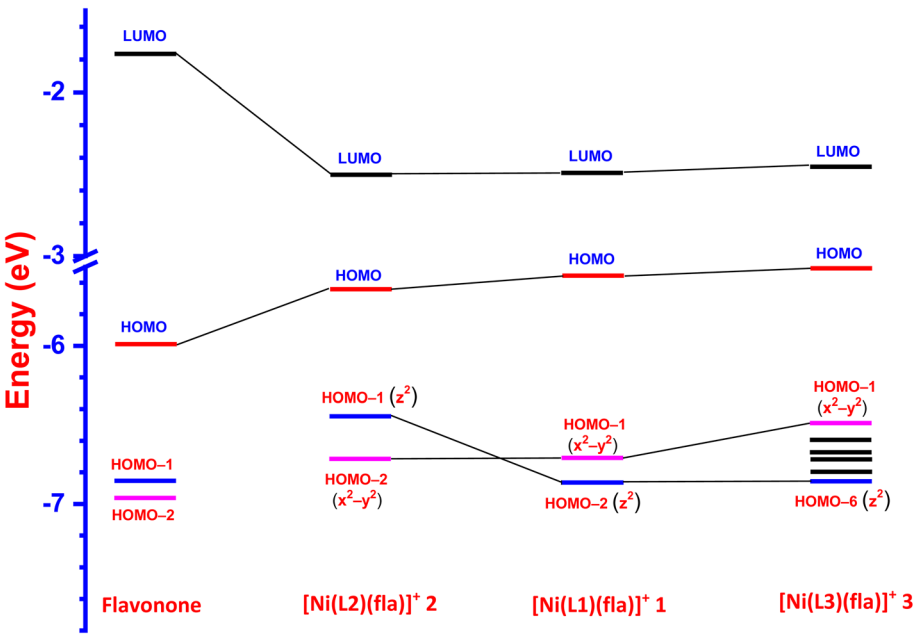

Fig. 4 LUMO and HOMO energy profile diagram for the ligand 3-hydroxyflavone and complexes **1–3**.

Electronic absorption spectral properties

The electronic absorption spectral data of all the Ni(II) complexes obtained in CH_3CN solvent are summarized in Table 3 and typical spectra of $[Ni(L)(CH_3CN)_2]^{2+}$ **1a–3a** and the flavonolate adducts $[Ni(L)(fla)]^+$ **1–3** are shown in Fig. 5. The complexes **1–3** exhibit an intense absorption band in the range 440–450 nm (ε, 3.1–5.6 $\times$ 10^4 M^{-1} cm^{-1}, Table 3, Fig. 5), which is assigned to the $\pi \rightarrow \pi^*$ transition within the coordinated flavonolate.[53] All these assignments are in good agreement with those observed for the previously reported octahedral Ni(II) complexes with $Ni^{II}N_6$ (ref. 30 and 31) and similar $Ni^{II}N_4O_2$ chromophores.[54] The band energy observed for **3** (446 nm) is lower than those for **1** and **2** (441 nm), which correlates with the trend in the HOMO (π) – LUMO (π^*) energy gap, **1** (3.056) > **2** (3.045) > **3** (3.029 eV) (Table 2, Fig. 3), revealing the influence of primary ligands on the coordinated fla^-. The shift in $\pi \rightarrow \pi^*$ band from that (458 nm) observed[15a] for free flavonolate anion of Me_4N[fla] is higher for **3** (12 nm) than that (17 nm) for **1** and **2**, confirming the influence of primary ligands on π-delocalization within fla^-. The lower shift observed for **3**, which is consistent with the higher asymmetry in fla^- coordination (*cf.* above), corresponds to higher π-delocalization within fla^- ring.[18] Hence, it is evident that the lower the shift in $\pi \rightarrow \pi^*$ band position the higher the disruption of π-delocalization within fla^-. All the complexes exhibit two well-defined ligand field (LF) absorption bands together with an absorption spectral feature in the low energy region in **1–3**. The lowest energy band observed in the range 929–1022 nm for **1–3** is assigned to $^3A_{2g} \rightarrow {}^3T_{2g}(F)$ (ν_1) transition in Ni(II) located in an octahedral environment. The higher energy band observed (528–582 nm) is assigned to $^3A_{2g} \rightarrow {}^3T_{1g}(F)$ (ν_2) transition while the feature located on the low energy side of ν_2 band is assigned to $^3A_{2g} \rightarrow {}^1E_{1g}(D)$ spin-forbidden transition.[30,31,44,54a] Upon adding fla^- to complexes **1a–3a**, the ν_1 and ν_2 bands are red-shifted (Table 3, Fig. 5), suggesting coordination of flavonolate to Ni(II).[30,31] Also, the trend in ν_1 band position reveals that the LF imposed on Ni(II) is weaker in **2** and **3**, which corresponds to the weaker coordination of L2 in **2**, and the ligand steric crowding around Ni(II) in **3**, which renders the Ni–N_{bzim} bonds weaker in solution.

Table 3 Electronic absorption spectral data for complexes in acetonitrile solution[a] at 25 °C

	Electronic absorption spectra	
Complex	Wavelength (nm)	ε (M^{-1} cm^{-1})
$[Ni(L1)(CH_3CN)_2](ClO_4)_2$ **1a**	858(ν_1)	280
	523(ν_2)	410 sh
	384(ν_3)[b]	
$[Ni(L2)(CH_3CN)(H_2O)](ClO_4)_2$ **2a**	936(ν_1)	270
	545(ν_2)	290 sh
	428(ν_3)[b]	
$[Ni(L3)(CH_3CN)_2](ClO_4)_2$ **3a**	932(ν_1)	110
	571(ν_2)	180 sh
	361(ν_3)[b]	
$[Ni(L1)(fla)](ClO_4)$ **1**	929(ν_1)	180
	528(ν_2)	370 sh
	441[b]	
$[Ni(L2)(fla)](ClO_4)$ **2**	1007(ν_1)	170
	582(ν_2)	264 sh
	441[b]	
$[Ni(L3)(fla)](ClO_4)$ **3**	1022(ν_1)	210
	580(ν_2)	510 sh
	446[b]	

[a] Conc. **1a**, **1**: 2.0 $\times$ 10^{-3} M; **2a**: 3.4 $\times$ 10^{-3} M; **2**: 3.3 $\times$ 10^{-3} M; **3a**: 3.9 $\times$ 10^{-3} M; **3**: 1.7 $\times$ 10^{-3} M. [b] Conc. **1a**, **1**: 1.3 $\times$ 10^{-4} M; **2a**, **2**, **3**: 1.4 $\times$ 10^{-4} M; **3a**: 3.9 $\times$ 10^{-3} M.

Redox studies

The electrochemical oxidation of the complexes **1–3** was investigated by using cyclic voltammetry (CV) and differential pulse voltammetry (DPV) (Table 4, Fig. 6, S1†). The irreversible oxidation process observed in the range, 0.770–0.800 V is assigned to oxidation of bound flavonolate (fla^-) to $fla^{\bullet}$ ($fla^-/fla^{\bullet}$ redox couple), as free H(fla) is found to exhibit an oxidation wave at 0.715 V (*vs.* SCE), and as the Ni(II)/Ni(III) redox couple is expected to occur at more positive potentials.[31b] The $E_{1/2}$ values from DPV follow the trend, H(fla) (0.715 V) > **3** (0.683 V) > **1** (0.657 V) < **2** (0.679 V *vs.* SCE). The $E_{1/2}$ values observed for fla^- are lower than that for H(fla), revealing that fla^- is destabilized towards oxidation to give $fla^{\bullet}$, upon coordination to Ni(II). The incorporation of Me group in **1** to obtain **2** sterically hinders the coordination of pyridyl nitrogen, lowers the energy of HOMO (*cf.* above), and renders the removal of electron from the HOMO more difficult and stabilizes fla^- towards oxidation more. Similarly, the bzim nitrogens in **3**, which are coordinated to Ni(II) more strongly than the py nitrogens in **1**, and raise the energy of HOMO (*cf.* above), are expected to facilitate the removal of electron from HOMO, and lower the oxidation potential. However, the observed oxidation potential of **3** is higher than that for **1**. The three bulky bzim nitrogens sterically crowd around Ni(II) in solution, as evident from the lower LF strength (*cf.* above), and possibly one of the weak Ni–N_{bzim} bonds is substituted by ClO_4^- available in high concentration, which lowers the HOMO energy and renders the removal of electron from HOMO more difficult. Thus, the removal of electron to form the radical $fla^{\bullet}$ intermediate and reactive $O_2^{\bullet-}$ is facilitated by the strong σ-bonding of primary ligands. This observation is reminiscent of Nature choosing carboxylate donor to coordinate to redox-inactive Ni(II), increase the electron density on it, and hence enhance the π-back bonding of Ni(II) with fla^-.

Study of degradation of Ni(II)-flavonolate adducts

The kinetics of reaction of the enzyme–substrate model complexes $[Ni(L)(fla)](ClO_4)$ **1–3** in DMF solution with dioxygen was monitored by following the decrease in absorption intensity of the $\pi \rightarrow \pi^*$ band (440–450 nm) upon exposure to atmospheric air or pure dioxygen. At room temperature and under atmospheric air, **1–3** did not show any measurable decrease in absorption intensity; however, when dioxygen was bubbled through the solution, the reaction proceeds slowly, with **1** and **3** reacting at almost the same rate. At a higher temperature (70 °C) and in the presence of atmospheric dioxygen, the reaction

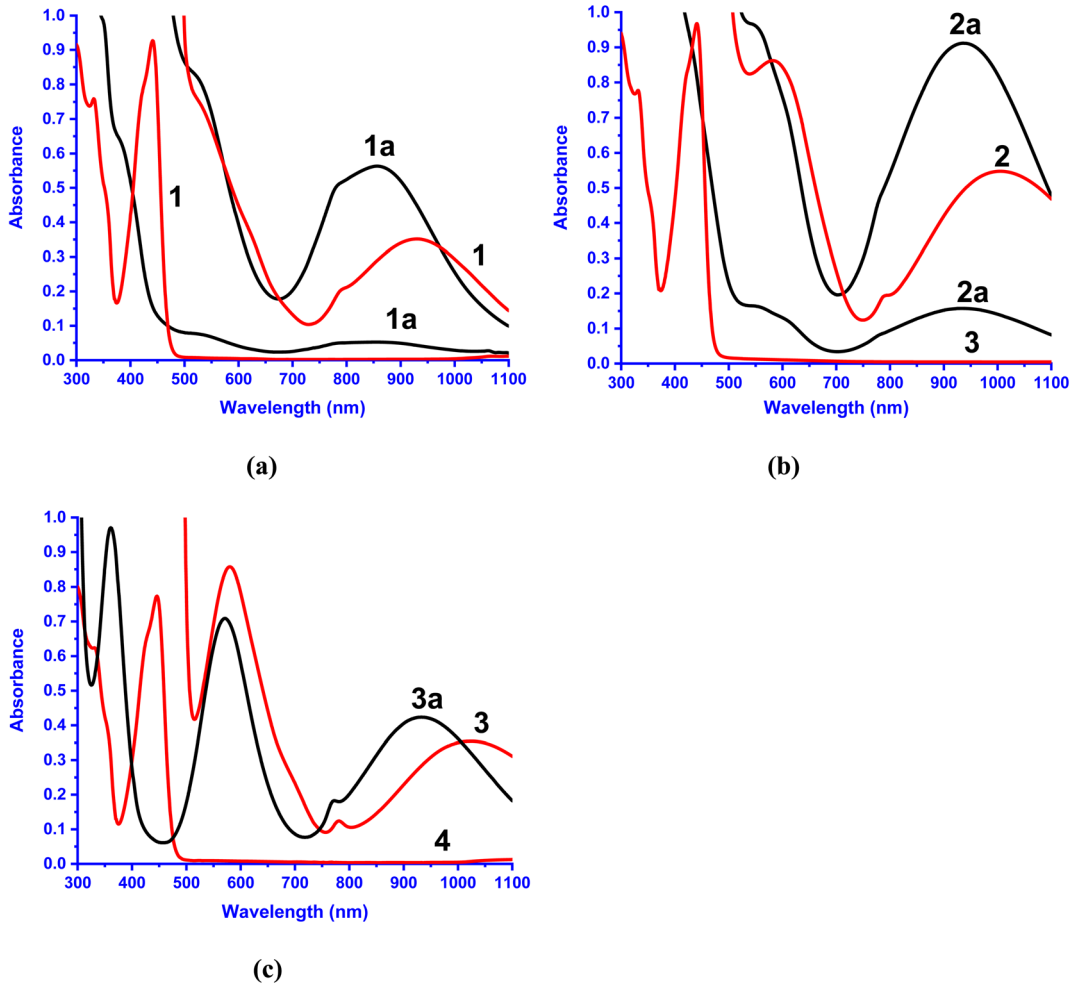

Fig. 5 Electronic absorption spectra of **1a–3a** and **1–3**. Conc. (a) **1a**, **1**: 2.0×10^{-3} M, 1.3×10^{-4} M; (b) **2a**: 3.4×10^{-3} M, 1.4×10^{-4} M, 1.3×10^{-4} M; **2**: 3.3×10^{-3} M, 1.4×10^{-4} M and (c) **3a**: 3.9×10^{-3} M; **3**: 1.7×10^{-3} M, 1.4×10^{-4} M in acetonitrile solution at 25 °C.

Table 4 Electrochemical data[a] of complexes **1–3** in DMF solution at 25 °C

	Cyclic voltammetry		DPV	
Complex	E_{pc} (V)	$E_{1/2}$ (V)	$E_{1/2}$ (V)	Redox process
Flavonone	0.795	0.725	0.715	HFla/Fla$^{\bullet}$
$[Ni(L1)(fla)]^+$ **1**	0.747	0.674	0.657	Fla$^-$/Fla$^{\bullet}$
$[Ni(L2)(fla)]^+$ **2**	0.773	0.695	0.679	Fla$^-$/Fla$^{\bullet}$
$[Ni(L3)(fla)]^+$ **3**	0.775	0.719	0.683	Fla$^-$/Fla$^{\bullet}$

[a] Add 0.252 V to convert NHE. Scan rate, 50 mV s^{-1}. Working electrode: glassy carbon, reference electrode: calomel electrode. Pulse width (ΔE), 0.050 V, DPV: $E_{1/2} = E_p + \Delta E/2$.

proceeds faster than at room temperature. The absorption intensity decreases to reach a minimum within 4–6 min for **1** and **3** (Fig. 7a and S10a†), and decreases slowly and then fast for **2** (Fig. S11a†). The decrease in intensity resembles that observed for the enzyme–substrate adduct,[55] and corresponds to degradation of Ni(II)-bound flavonolate. But, when dioxygen is bubbled through the solutions at 70 °C, the reaction proceeds faster, confirming that the reaction rate is dependent upon dioxygen concentration. Under the reaction conditions with excess dioxygen, the pseudo-first order rate constant k_{obs} was calculated from the slope of the plot of $\ln\{(A_t\text{-}A_\infty)/(A_0\text{-}A_\infty)\}$ *vs.* time (Fig. 7 and S9–S11†). The kinetic data and the values of k_{obs} and k_{O_2} ($= k_{obs}/[O_2]$) are collected in Table 5. At 70 °C (pure O_2), the rate of dioxygenolysis (k_{O_2}) calculated based on the initial decrease in intensity varies as: **1** (16.67 ± 0.70) > **2** (1.81 ± 0.04) < **3** ($29.10 \pm 0.16 \times 10^{-1}$ M^{-1} s^{-1}). Thus, **3** reacts almost twice faster than **1**, and nearly 25 times faster than **2**. The GC-MS analysis of the final colorless reaction mixture obtained for **1–3** (Fig. S12, Table S12†) reveals the ultimate products (Scheme 4) as salicylic acid [*m*/*z* (neg): 136, $[(M - 2H)^-]$ (20–60%) and benzoic acid (*m*/*z* (neg): 122 $[(M)^+]$ (21–43%).

The observed trend in rates of dioxygenolysis can be illustrated by invoking the reaction mechanism proposed in Scheme 5, which involves formation of the intermediates **A–D**. A similar mechanism has been already proposed for certain Ni(II)-flavonolate complexes.[18,28] The first step in the reaction mechanism involves dioxygen abstracting an electron from the π-orbital on C1 carbon bearing electron-rich enolate to form the

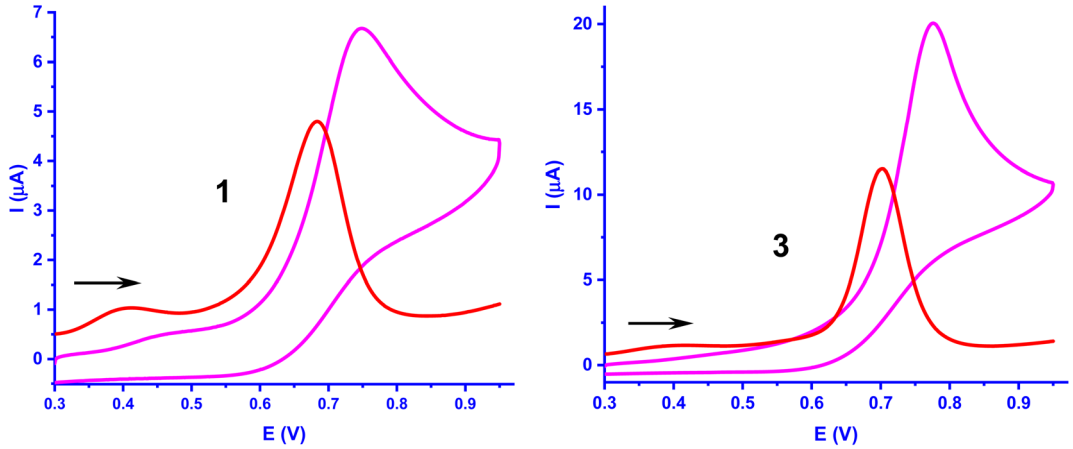

Fig. 6 Cyclic voltammogram and DPV of complexes **1** and **3** (1.0×10^{-3} M) in DMF at 25 °C. Conditions: supporting electrolyte, 0.1 M TBAP; scan rate, CV, 50 mV s^{-1} and DPV, 2 mV s^{-1} for all complexes, reference electrode, calomel electrode; working electrode, glassy carbon; counter electrode, platinum wire.

intermediate $[Ni(L)(fla^{\bullet})]^{2+}$ **A** and $O_2^{\bullet-}$ radical. This step is considered the rate-determining step as it involves activation of dioxygen. The unpaired electron on the benzylic C3 carbon (Scheme 3) in **A** is significantly stabilized by delocalization into the electron-sink phenyl group and on to C1 and C2 atoms (*cf.* below). The electron density in the Ni(II)–O1(enolate) oxygen in **A** is then transferred to C1 carbon to form the Ni(II)-bound carbonyl group. In the next step, the reactive $O_2^{\bullet-}$ immediately attacks the C3 carbon carrying the unpaired electron to form the peroxide radical **B**. Then the peroxide radical immediately attacks the C2 carbon in **B** to form the bridging peroxide intermediate **C** with Ni(II) weakly bound to C–O(enolate). In the third step, the unstable bicyclic species **C** undergoes homolysis at the two weaker C–C bonds adjacent to the carbonyl group, generating the diradical **D** and releasing the CO. The diradical **D** is stabilized by delocalization of electron density into the phenyl ring and the Ni(II)-bound enolate oxygen as well. In the penultimate step, the peroxo group undergoes homolysis to form substituted (benzoyloxy)benzoic acid **E** as the desired product and regenerate the Ni(II) complex. In the presence of traces of water, the depside **E** readily undergoes hydrolysis to produce benzoic acid and salicylic acid.

Table 5 The kinetic data[a,b] for dioxygenation of Ni(II)-bound flavonol in DMF as solvent using dioxygen at 70 °C

Compound	k_{obs} ($\times 10^{-3}$ s^{-1})	k_{O_2} ($\times 10^{-1}$ M^{-1} s^{-1})
$[Ni(L1)(fla)]ClO_4$ **1**	8.10 ± 0.40	16.67 ± 0.70
$[Ni(L2)(fla)]ClO_4$ **2**	0.88 ± 0.02	1.81 ± 0.04
	3.27 ± 0.27[c]	6.73 ± 0.56[c]
$[Ni(L3)(fla)]ClO_4$ **3**	14.14 ± 0.20	29.10 ± 0.16

[a] Dioxygen filled in a balloon as an external dioxygen source. [b] Conc. of dioxygen in DMF solution,[41] 4.86×10^{-3} M. [c] Calculated rate for the changes obtained after 33 min.

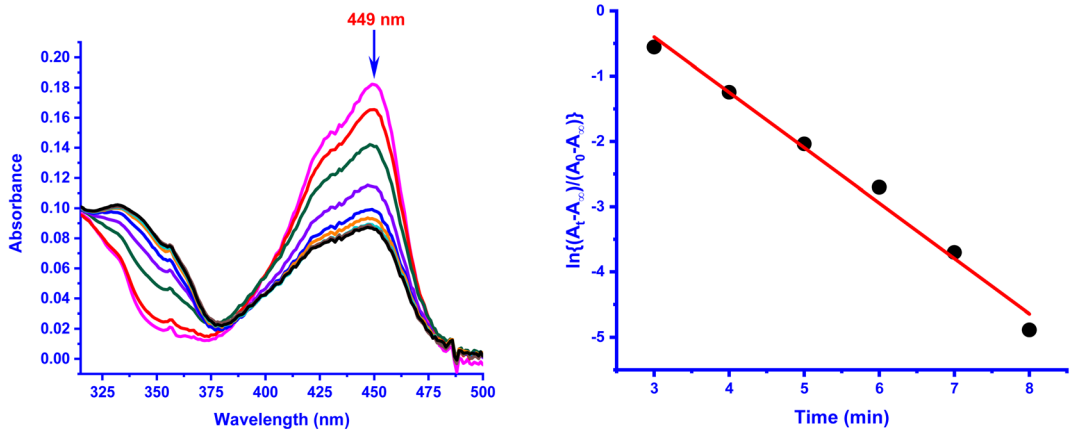

(a) (b)

Fig. 7 (a) UV-vis spectral changes observed in the presence of O_2 in DMF solution of $[Ni(L3)(fla)]ClO_4$ **3** (1×10^{-4} M) at 70 °C; (b) plot of $\ln\{(A_t - A_\infty)/(A_0 - A_\infty)\}$ *vs.* time for the band observed at 449 nm.

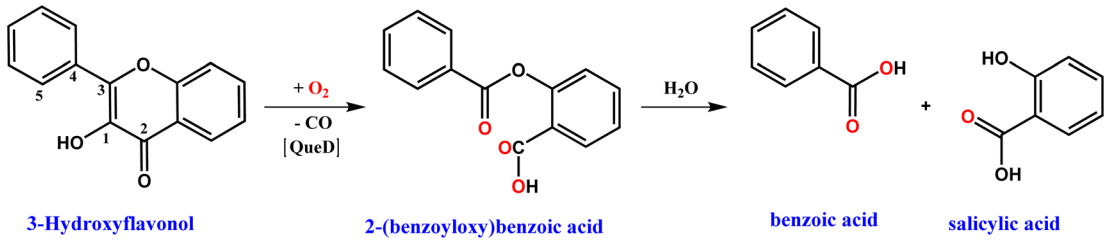

Scheme 4 Dioxygenation of 3-hydroxyflavonol and subsequent hydrolysis of depside to products, catalyzed by complexes **1–3**.

The formation of superoxide ion during the reaction has been demonstrated by performing the nitro blue tetrazolium (NBT^{2+}) test which involves treating one equivalent of **3** with two equivalents of NBT^{2+} under nitrogen and then exposing the reaction mixture to dioxygen at 70 °C. The appearance of a band at 520 nm (Fig. S5†) characteristic of monoformazan species (MF^{+}) reveals the *in situ* production of superoxide radical which reduces NBT^{2+} to give MF^{+}.[56] Also, when the reaction was performed in the presence of small amount of the free radical scavenger DMSO the reaction did not proceed,[57] lending strong support to the involvement of superoxide in the reaction mechanism proposed. To understand the extent of delocalization of π-electrons into Ni(II)-bound $fla^{\bullet}$, the electronic structures of the intermediate radicals **1A–3A** have been computed and optimized using DFT method (Fig. S8, Tables S10 and S11†). Upon radical formation, the Ni–O1 (2.047–2.102 Å) and Ni–O2 (2.105–2.135 Å) coordinate bonds become weaker, and the C1–O1 and C=O2 bonds become stronger, revealing that $fla^{\bullet}$ is weakly bound and has become susceptible to undergo homolytic cleavage at the weaker C1–C2 and C1–C3 bonds (Scheme 6, S1†). Also, the HOMOs of the intermediates have become significantly lower in energy (1.246–1.356 eV) than those of the reactants, but remain still higher in energy than the MOs. This reveals significant stabilization of the oxidized radical species (Scheme 6b, S1, Fig. S6, S7, Tables S8 and S9†), possibly due to delocalization of unpaired electron density over C1 and C2 carbons and the phenyl ring (Scheme S1†). Also, the trend in HOMO energy, *viz.*, **3A** > **1A** ≈ **2A** is similar to that of the reactants, *viz.*, **3** > **1** > **2**.

The trend in the rate of dioxygenation observed for **1–3** can be illustrated by invoking the above reaction mechanism. Thus, the increase in electron density on Ni(II) by the more basic bzim nitrogens and the electron-releasing *N*-Et substituent in **3** enhance the π-back bonding of Ni(II) with the antibonding π* orbital of C=O of fla^{-} (*cf.* above), raise the energy of HOMO and facilitate the rate-determining step of electron abstraction by dioxygen. In other words, the higher asymmetric coordination of fla^{-} (*cf.* above) causes decrease in π-delocalization in fla^{-} ring, activates it towards dioxygen and accounts for the highest dioxygenation rate of **3**. Also, the weaker C1–C2 bond in **3**, arising from the stronger π-back bonding of Ni(II) and the weaker C1–C2 and C1–C3 bonds in **3A**, facilitate the homolytic cleavage of the peroxide intermediate C in **3** more than that in **1**. A similar enhancement in reaction rate has been observed[23] for $[Ni^{II}(L)(fla)]$, due to the π-back bonding of Ni(II) with C=O and synergistic σ-bonding of the enolate group to Ni(II) when electron-releasing *p*-OMe group is incorporated in the tripodal pyridyl ligand (*cf.* above). Also, it may be noted that the incorporation of –OMe group on the phenyl ring of the flavonolate increases the rate of degradation of [K(fla)] while that of –CN group decreases it.[45] The sterically hindering 6-Me groups in **2** weaken the coordination of L2 to Ni(II), resulting in its HOMO to

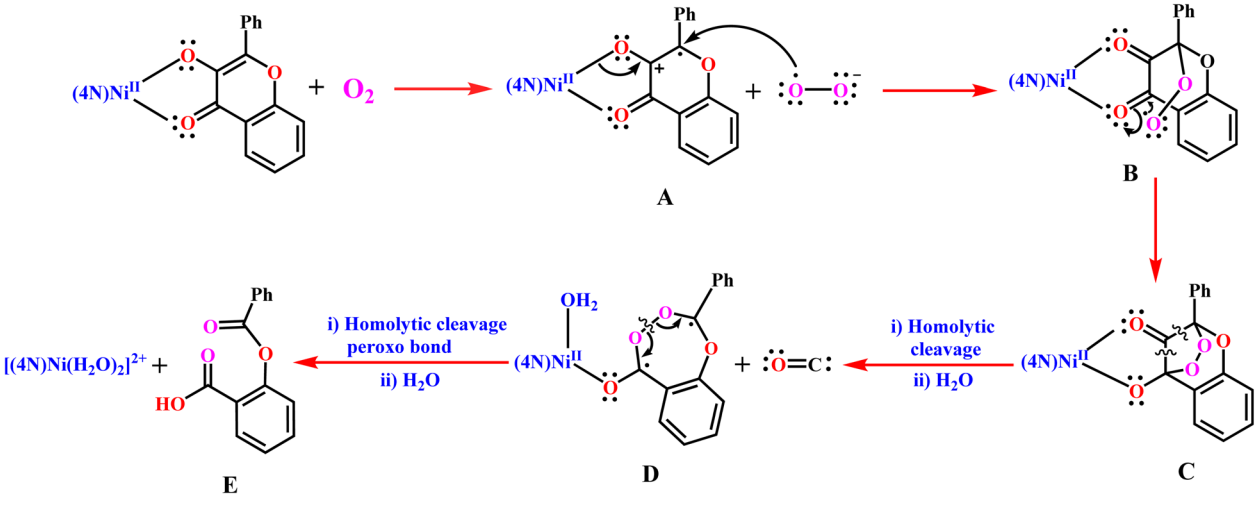

Scheme 5 Proposed reaction mechanism for Ni(II)-flavonolate adducts **1–3** as quercetin 2,4-dioxygenase enzyme models.

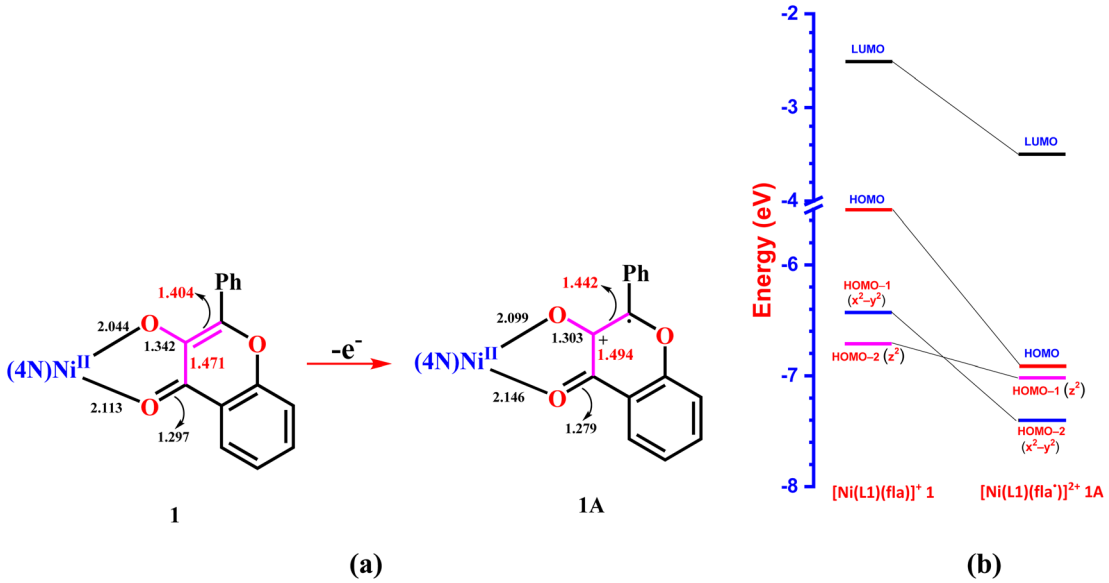

Scheme 6 Changes in bond lengths (a) and energies of molecular orbitals (b) upon removal of an electron from Ni(II)-bound flavonolate in **1** to form the intermediate radical **1A**.

be more stable than that of **1** (*cf.* above), causing the abstraction of electron from **2** to obtain **2A** more difficult; this illustrates that **2** undergoes degradation at a rate lower than **1**, which is consistent with the lower asymmetry in bonding of flavonolate (*cf.* above). Very recently, Mandal *et al.*[58] and Sun *et al.*[16,23] have illustrated the trends in reactivity of certain Cu(II)-flavonolate adducts and the substituent effects on the basis of the torsion angles calculated from solid state X-ray structures.[58] However, for the present complexes, the trends in the low values of twist angles obtained from X-ray structures of **1** and **3**, and those calculated for **1–3**, fail to correlate well with the dioxygenation rates.

Thus, both the computational and experimental results illustrate the trend in rates of the enzyme-type dioxygenation of the present functional models designed for Ni(II)-containing 2,4-QueD, and support the proposed reaction mechanism, particularly, the radical formation by abstraction of an electron from the carbon carrying the coordinated hydroxyl group, and the stabilization of benzylic radical by the electron-sink phenyl ring. Also, the X-ray structures of **1** and **3** lend support to the enolate-one to one-enolate shift in bonding in the flavonolate during dioxygenation, as tuned by the redox-inactive Ni(II) involved in π-back bonding with the C=O group and the synergistic σ-bonding of the enolate group of flavonolate to Ni(II). This is similar to the bonding in carbonyls like $[Ni(CO)_4]$. Thus, a metal carbonyl like $[Ni(CO)_4]$ owes its strong metal coordination to π-back bonding and synergistic σ-bonding through the same carbon atom while the flavonolate owes its decreased π-delocalization in the aromatic ring and hence activation to involvement of the conjugated carbonyl group in π-back bonding from Ni(II) and that of enolate oxygen atom in synergistic σ-bonding to Ni(II). Thus, the strong σ-bonding of more basic bzim nitrogen and electron-releasing *N*-Et-bzim decrease the π-delocalization in the aromatic flavonolate ring, leading to higher rates of degradation. This observation is reminiscent of the higher rate of degradation of enzyme–substrate complex on account of electron-releasing effect of the N-Glu carboxylate bound to Ni(II) in the active site. This supports the role of redox-inactive Ni(II) in the enzyme–substrate model complex by involving in π-back bonding, delocalizing π-electron density into fla^- and activating it towards oxidation.

Conclusions

To conclude, three new Ni(II)-flavonolate complexes of the type $[Ni(L)(fla)]^+$, where L is a tripodal 4N ligand with three pyridyl/benzimidazolyl nitrogen donors, have been isolated as structural and functional models for the Ni(II)-containing quercetin 2,4-dioxygenase (2,4-QueD) enzymes. Single crystal X-ray structures of two flavonolate adducts contain a NiN_4O_2 coordination sphere with distorted octahedral geometry. They reveal that Ni(II) is involved in π-back bonding with flavonolate and the latter in synergistic σ-bonding with Ni(II). The DFT optimized structures of the complexes and their geometric isomers have been obtained. The HOMO and LUMO orbitals localized on Ni(II)-bound flavonolate are highly conjugated π-bonding and antibonding π*-orbitals respectively. They are located higher in energy than the Ni(II)-based MOs (HOMO–1, $d_{x^2-y^2}$; HOMO–2/6, d_{z^2}), revealing that Ni(II)-bound flavonolate rather than Ni(II) undergoes oxidation upon exposure to dioxygen. The energies of HOMO, in combination with spectral and electrochemical studies, illustrate the potential of the tripodal ligands to coordinate to Ni(II) and facilitate the conversion of Ni-enolate to Ni-one bond enabling release of CO from the activated substrate. The highest dioxygenase reactivity of the flavonolate adduct with *N*-Et-bzim moiety is on account of the more basic bzim and electron-releasing *N*-Et substituent on it, which leads to

enhanced π-back bonding of Ni(II) with flavonolate, causing decreased π-delocalization in the substrate and hence its activation. This observation is reminiscent of Ni(II)-carboxylate coordination in the enzyme active site, which promotes the reaction remarkably by electron-release into the π-delocalized flavonolate substrate through π-back bonding with Ni(II).

Conflicts of interest

There are no conflicts to declare.

Acknowledgements

We gratefully acknowledge the financial support by SERB, New Delhi (EMR/2015/002222) and INSA, New Delhi, for the INSA Senior Scientist position to M. P. HRMS facility was sanctioned to School of Chemistry, Bharathidasan University through DST-FIST. And, we thank Professor Dr Nashreen S. Islam and Dr Ms Mitu Sharma, Tezpur University, Tezpur for collecting the X-ray data and Professor M. Velusamy, NEHU, Shillong for his help in solving the X-ray structures.

References

1 P. Pietta, C. Gardana and A. Pietta, *Oxid. Stress*, 2003, **9**, 43–70.

2 S. Tranchimand, P. Brouant and G. Iacazio, *Biodegradation*, 2010, **21**, 833–859.

3 (*a*) K. C. Ryan, O. E. Johnson, D. E. Cabelli, T. C. Brunold and M. J. Maroney, *J. Biol. Inorg. Chem.*, 2010, **15**, 795–807; (*b*) M. Sparta, C. E. Valdez and A. N. Alexandrova, *J. Mol. Biol.*, 2013, **425**, 3007–3018; (*c*) B. Desguin, P. Goffin, E. Viaene, M. Kleerebezem, V. Martin-Diaconescu, M. J. Maroney, J. P. Declercq, P. Soumillion and P. Hols, *Nat. Commun.*, 2014, **5**, 3615.

4 (*a*) S. L. Chen, M. R. Blomberg and P. E. Siegbahn, *Phys. Chem. Chem. Phys.*, 2014, **16**, 14029–14035; (*b*) K. C. Ryan, A. I. Guce, O. E. Johnson, T. C. Brunold, D. E. Cabelli, S. C. Garman and M. J. Maroney, *Biochemistry*, 2015, **54**, 1016–1027.

5 (*a*) E. A. Lewis and W. B. Tolman, *Chem. Rev.*, 2004, **104**, 1047–1076; (*b*) L. M. Mirica, X. Ottenwaelder and T. D. P. Stack, *Chem. Rev.*, 2004, **104**, 1013–1046; (*c*) F. Fusetti, K. H. Schröter, R. A. Steiner, P. I. van Noort, T. Pijning, H. J. Rozeboom, K. H. Kalk, M. R. Egmond and B. W. Dijkstra, *Structure*, 2002, **10**, 259–268; (*d*) R. A. Steiner, K. H. Kalk and B. W. Dijkstra, *Proc. Natl. Acad. Sci. U. S. A.*, 2002, **99**, 16625–16630.

6 (*a*) I. M. Kooter, R. A. Steiner, B. W. Dijkstra, P. I. van Noort, M. R. Egmond and M. Huber, *Eur. J. Biochem.*, 2002, **269**, 2971–2979; (*b*) R. A. Steiner, I. M. Kooter and B. W. Dijkstra, *Biochemistry*, 2002, **41**, 7955–7962.

7 (*a*) E. I. Solomon, D. E. Heppner, E. M. Johnston, J. W. Ginsbach, J. Cirera, M. Qayyum, M. T. Kieber-Emmons, C. H. Kjaergaard, R. G. Hadt and L. Tian, *Chem. Rev.*, 2014, **114**, 3659–3853; (*b*) R. Trammell, K. Rajabimoghadam and I. Garcia-Bosch, *Chem. Rev.*, 2019, **119**, 2954–3031; (*c*) J. B. Vincent, G. L. Olivier-Lilley and B. A. Averill, *Chem. Rev.*, 1990, **90**, 1447–1467; (*d*) J. D. Lipscomb, *Annu. Rev. Microbiol.*, 1994, **48**, 371–399; (*e*) A. L. Feig and S. J. Lippard, *Chem. Rev.*, 1994, **94**, 759–805; (*f*) B. J. Wallar and J. D. Lipscomb, *Chem. Rev.*, 1996, **96**, 2625–2658; (*g*) M. Costas, K. Chen and L. Que, *Coord. Chem. Rev.*, 2000, **200–202**, 517–544; (*h*) M. H. Baik, M. Newcomb, R. A. Friesner and S. J. Lippard, *Chem. Rev.*, 2003, **103**, 2385–2419.

8 (*a*) M. Costas, M. P. Mehn, M. P. Jensen and L. Que Jr, *Chem. Rev.*, 2004, **104**, 939–986; (*b*) E. Y. Tshuva and S. J. Lippard, *Chem. Rev.*, 2004, **104**, 987–1012; (*c*) S. V. Kryatov, E. V. Rybak-Akimova and S. Schindler, *Chem. Rev.*, 2005, **105**, 2175–2226; (*d*) L. Que Jr, *Acc. Chem. Res.*, 2007, **40**, 493–500; (*e*) W. Nam, *Acc. Chem. Res.*, 2007, **40**, 522–531; (*f*) E. P. Talsi and K. P. Bryliakov, *Coord. Chem. Rev.*, 2012, **256**, 1418–1434; (*g*) K. P. Bryliakov and E. P. Talsi, *Coord. Chem. Rev.*, 2014, **276**, 73–96; (*h*) M. Sallmann and C. Limberg, *Acc. Chem. Res.*, 2015, **48**, 2734–2743; (*i*) A. J. Jasniewski and L. Que Jr, *Chem. Rev.*, 2018, **118**, 2554–2592; (*j*) O. Y. Lyakin, K. P. Bryliakov and E. P. Talsi, *Coord. Chem. Rev.*, 2019, **384**, 126–139.

9 D. Nianios, S. Thierbach, L. Steimer, P. Lulchev, D. Klostermeier and S. Fetzner, *BMC Biochem.*, 2015, **16**, 10.

10 J. Kaizer, É. Balogh-Hergovich, M. Czaun, T. Csay and G. Speier, *Coord. Chem. Rev.*, 2006, **250**, 2222–2233.

11 J. S. Pap, J. Kaizer and G. Speier, *Coord. Chem. Rev.*, 2010, **254**, 781–793.

12 J. Kaizer, G. Baráth, J. Pap, G. Speier, M. Giorgi and M. Réglier, *Chem. Commun.*, 2007, 5235–5237, DOI: **10.1039/b711864c**.

13 G. Baráth, J. Kaizer, G. Speier, L. Párkányi, E. Kuzmann and A. Vértes, *Chem. Commun.*, 2009, 3630–3632, DOI: **10.1039/b903224j**.

14 (*a*) A. Nishinaga, N. Numada and K. Maruyama, *Tetrahedron Lett.*, 1989, **30**, 2257–2258; (*b*) A. Nishinaga, T. Tojo and T. Matsurra, *J. Chem. Soc., Chem. Commun.*, 1974, **952**, 896–897.

15 (*a*) K. Grubel, K. Rudzka, A. M. Arif, K. L. Klotz, J. A. Halfen and L. M. Berreau, *Inorg. Chem.*, 2010, **49**, 82–96; (*b*) K. Grubel, A. R. Marts, S. M. Greer, D. L. Tierney, C. J. Allpress, S. N. Anderson, B. J. Laughlin, R. C. Smith, A. M. Arif and L. M. Berreau, *Eur. J. Inorg. Chem.*, 2012, **2012**, 4750–4757.

16 (*a*) Y. J. Sun, Q. Q. Huang, T. Tano and S. Itoh, *Inorg. Chem.*, 2013, **52**, 10936–10948; (*b*) Y. J. Sun, Q. Q. Huang, P. Li and J. J. Zhang, *Dalton Trans.*, 2015, **44**, 13926–13938.

17 A. Matuz, M. Giorgi, G. Speier and J. Kaizer, *Polyhedron*, 2013, **63**, 41–49.

18 S. Hoof and C. Limberg, *Inorg. Chem.*, 2019, **58**, 12843–12853.

19 Y. Dai, T. C. Pochapsky and R. H. Abeles, *Biochemistry*, 2001, **40**, 6379–6387.

20 (*a*) S. W. Ragsdale, *J. Biol. Chem.*, 2009, **284**, 18571–18575; (*b*) J. L. Boer, S. B. Mulrooney and R. P. Hausinger, *Arch. Biochem. Biophys.*, 2014, **544**, 142–152; (*c*)

M. Sankaralingam, M. Balamurugan and M. Palaniandavar, *Coord. Chem. Rev.*, 2020, **403**, 213085.
21 B. Gopal, L. L. Madan, S. F. Betz and A. A. Kossiakoff, *Biochemistry*, 2005, **44**, 193–201.
22 J. H. Jeoung, D. Nianios, S. Fetzner and H. Dobbek, *Angew. Chem., Int. Ed.*, 2016, **55**, 3281–3284.
23 Y. J. Sun, Q. Q. Huang and J. J. Zhang, *Dalton Trans.*, 2014, **43**, 6480–6489.
24 P. Holze, T. Corona, N. Frank, B. Braun-Cula, C. Herwig, A. Company and C. Limberg, *Angew. Chem., Int. Ed.*, 2017, **56**, 2307–2311.
25 S. Hoof and C. Limberg, *Z. Anorg. Allg. Chem.*, 2019, **645**, 170–174.
26 W. J. Wang, W. J. Wei and R. Z. Liao, *Phys. Chem. Chem. Phys.*, 2018, **20**, 15784–15794.
27 H. Li, X. Wang, G. Tian and Y. Liu, *Catal. Sci. Technol.*, 2018, **8**, 2340–2351.
28 D. Jeong, S. Sun, D. Moon and J. Cho, *J. Inorg. Biochem.*, 2022, **226**, 111632.
29 (*a*) M. Balamurugan, E. Suresh and M. Palaniandavar, *Dalton Trans.*, 2016, **45**, 11422–11436; (*b*) M. Sankaralingam and M. Palaniandavar, *Polyhedron*, 2014, **67**, 171–180; (*c*) R. Viswanathan, M. Palaniandavar, P. Prabakaran and P. T. Muthiah, *Inorg. Chem.*, 1998, **37**, 3881–3884.
30 M. Balamurugan, R. Mayilmurugan, E. Suresh and M. Palaniandavar, *Dalton Trans.*, 2011, **40**, 9413–9424.
31 (*a*) M. Sankaralingam, P. Vadivelu, E. Suresh and M. Palaniandavar, *Inorg. Chim. Acta*, 2013, **407**, 98–107; (*b*) M. Sankaralingam, M. Balamurugan, M. Palaniandavar, P. Vadivelu and C. H. Suresh, *Chem.–Eur. J.*, 2014, **20**, 11346–11361; (*c*) M. Sankaralingam, P. Vadivelu and M. Palaniandavar, *Dalton Trans.*, 2017, **46**, 7181–7193.
32 (*a*) G. J. Britovsek, J. England and A. J. White, *Inorg. Chem.*, 2005, **44**, 8125–8134; (*b*) A. G. Blackman, *Eur. J. Inorg. Chem.*, 2008, **2008**, 2633–2647.
33 V. McKee, M. Zvagulis, J. V. Dagdigian, M. G. Patch and C. A. Reed, *J. Am. Chem. Soc.*, 1984, **106**, 4765–4772.
34 M. Inosako, A. Kunishita, M. Kubo, T. Ogura, H. Sugimoto and S. Itoh, *Dalton Trans.*, 2009, 9410–9417, DOI: **10.1039/b910237j**.
35 J.-W. Wang, H.-H. Huang, J.-K. Sun, D.-C. Zhong and T.-B. Lu, *ACS Catal*, 2018, **8**, 7612–7620.
36 G. M. Sheldrick, *Acta. Crystallogr. A*, 2015, **71**, 3–8.
37 M. N. Burnett and C. K. Johnson, *ORTEP-III: Oak Ridge thermal ellipsoid plot program for crystal structure illustrations*, Oak ridge national laboratory report ORNL-6895, Tennessee, 1996.
38 G. W. T. M. J. Frisch, H. B. Schlegel, G. E. Scuseria, M. A. Robb, J. R. Cheeseman, G. Scalmani, V. Barone, B. Mennucci, G. A. Petersson, H. Nakatsuji, M. Caricato, X. Li, H. P. Hratchian, A. F. Izmaylov, J. Bloino, G. Zheng, J. L. Sonnenberg, M. Hada, M. Ehara, K. Toyota, R. Fukuda, J. Hasegawa, M. Ishida, T. Nakajima, Y. Honda, O. Kitao, H. Nakai, T. Vreven, J. A. Montgomery Jr, J. E. Peralta, F. Ogliaro, M. Bearpark, J. J. Heyd, E. Brothers, K. N. Kudin, V. N. Staroverov, R. Kobayashi, J. Normand, K. Raghavachari, A. Rendell, J. C. Burant, S. S. Iyengar, J. Tomasi, M. Cossi, N. Rega, J. M. Millam, M. Klene, J. E. Knox, J. B. Cross, V. Bakken, C. Adamo, J. Jaramillo, R. Gomperts, R. E. Stratmann, O. Yazyev, A. J. Austin, R. Cammi, C. Pomelli, J. W. Ochterski, R. L. Martin, K. Morokuma, V. G. Zakrzewski, G. A. Voth, P. Salvador, J. J. Dannenberg, S. Dapprich, A. D. Daniels, Ö. Farkas, J. B. Foresman, J. V. Ortiz, J. Cioslowski and D. J. Fox, Gaussian, Inc., Wallingford CT, 2009, 121, pp. 150–166–.
39 A. D. Becke, *J. Chem. Phys.*, 1993, **98**, 1372–1377.
40 (*a*) P. J. Hay and W. R. Wadt, *J. Chem. Phys.*, 1985, **82**, 270–283; (*b*) P. J. Hay and W. R. Wadt, *J. Chem. Phys.*, 1985, **82**, 299–310.
41 M. Velusamy, R. Mayilmurugan and M. Palaniandavar, *Inorg. Chem.*, 2004, **43**, 6284–6293.
42 (*a*) L. K. Thompson, B. S. Ramaswamy and R. D. Dawe, *Can. J. Chem.*, 1978, **56**, 1311–1318; (*b*) J.-L. Tian, M.-J. Xie, Z.-Q. Liu, S.-P. Yan, D.-Z. Liao and Z.-H. Jiang, *J. Coord. Chem.*, 2005, **58**, 833–840.
43 É. Balogh-Hergovich, J. Kaizer, J. Pap, G. Speier, G. Huttner and L. Zsolnai, *Eur. J. Inorg. Chem.*, 2002, **2002**, 2287–2295.
44 M. Velusamy, M. Palaniandavar and K. R. Justin Thomas, *Polyhedron*, 1998, **17**, 2179–2186.
45 L. Barhács, J. Kaizer and G. Speier, *J. Org. Chem.*, 2000, **65**, 3449–3452.
46 H. Wu, K. Li, T. Sun, B. Liu, F. Jia, J. Yuan and G. Chen, *Z. Naturforsch. B*, 2010, **65**, 1341–1348.
47 D. D. Perrin, B. Dempsey and E. P. Serjeant, *pK_a prediction for organic acids and bases*, Springer, 1981.
48 T. Ajaykamal, M. Sharma, N. S. Islam and M. Palaniandavar, *Dalton Trans.*, 2021, **50**, 8045–8056.
49 (*a*) T. Kusamoto, S. Kume and H. Nishihara, *J. Am. Chem. Soc.*, 2008, **130**, 13844–13845; (*b*) Y. Wang, H. Zhang, M. Pink, A. Olankitwanit, S. Rajca and A. Rajca, *J. Am. Chem. Soc.*, 2016, **138**, 7298–7304; (*c*) A. Kumar and M. D. Sevilla, *J. Phys. Chem. B*, 2018, **122**, 98–105; (*d*) S. Kasemthaveechok, L. Abella, M. Jean, M. Cordier, T. Roisnel, N. Vanthuyne, T. Guizouarn, O. Cador, J. Autschbach, J. Crassous and L. Favereau, *J. Am. Chem. Soc.*, 2020, **142**, 20409–20418.
50 (*a*) H. Guo, Q. Peng, X. K. Chen, Q. Gu, S. Dong, E. W. Evans, A. J. Gillett, X. Ai, M. Zhang, D. Credgington, V. Coropceanu, R. H. Friend, J. L. Brédas and F. Li, *Nat. Mater.*, 2019, **18**, 977–984; (*b*) L. Abella, J. Crassous, L. Favereau and J. Autschbach, *Chem. Mater.*, 2021, **33**, 3678–3691; (*c*) Z. Wang, R. Murata and M. Abe, *ACS Omega*, 2021, **6**, 22773–22779.
51 B. L. Westcott, N. E. Gruhn, L. J. Michelsen and D. L. Lichtenberger, *J. Am. Chem. Soc.*, 2000, **122**, 8083–8084.
52 N. Saravanan, T. Ajaykamal and M. Palaniandavar, *Communicated*, 2023.
53 L. Jurd and T. A. Geissman, *J. Org. Chem.*, 1956, **21**, 1395–1401.
54 (*a*) A. P. Lever, *Studies in physical theoretical chem*, 1984, p. 33; (*b*) M. S. Kryatova, O. V. Makhlynets, A. Y. Nazarenko and E. V. Rybak-Akimova, *Inorg. Chim. Acta*, 2012, **387**, 74–80; (*c*) T. R. Holman, M. P. Hendrich and L. Que, *Inorg. Chem.*, 1992, **31**, 937–939.

55 D. W. S. Westlake, J. M. Roxburgh and G. Talbot, *Nature*, 1961, **189**, 510–511.
56 B. H. Bielski, G. G. Shiue and S. Bajuk, *J. Phys. Chem.*, 1980, **84**, 830–833.
57 R. Jangir, M. Ansari, D. Kaleeswaran, G. Rajaraman, M. Palaniandavar and R. Murugavel, *ACS Catal.*, 2019, **9**, 10940–10950.
58 N. Podder, S. Dey, A. Anoop and S. Mandal, *Dalton Trans.*, 2022, **51**, 4338–4353.